Atmos. Chem. Phys. Discuss., 8, 16981–17036, 2008
www.atmos-chem-phys-discuss.net/8/16981/2008/

Atmospheric Chemistry and Physics Discussions

This discussion paper is/has been under review for the journal *Atmospheric Chemistry and Physics (ACP)*. Please refer to the corresponding final paper in *ACP* if available.

Evaluating the performance of pyrogenic and biogenic emission inventories against one decade of space-based formaldehyde columns

T. Stavrakou[1], J.-F. Müller[1], I. De Smedt[1], M. Van Roozendael[1], G. R. van der Werf[2], L. Giglio[3], and A. Guenther[4]

[1]Belgian Institute for Space Aeronomy, Avenue Circulaire 3, 1180, Brussels, Belgium
[2]Faculty of Earth and Life Sciences, Vrije Universiteit Amsterdam, De Boelelaan 1085, 1081 HV Amsterdam, The Netherlands
[3]Science Systems and Applications, Inc. NASA Goddard Space Flight Center, Greenbelt, MD 20771, USA
[4]National Center for Atmospheric Research, Boulder, CO 80303, USA

Received: 10 July 2008 – Accepted: 14 August 2008 – Published: 10 September 2008

Correspondence to: T. Stavrakou (jenny@aeronomie.be)

Published by Copernicus Publications on behalf of the European Geosciences Union.

Abstract

A new one-decade dataset of formaldehyde (HCHO) columns retrieved from GOME and SCIAMACHY is compared with HCHO columns simulated by an updated version of the IMAGES global chemical transport model. This model version includes an optimized chemical scheme with respect to HCHO production, where the short-term and final HCHO yields from pyrogenically emitted non-methane volatile organic compounds (NMVOCs) are estimated from the Master Chemical Mechanism (MCM) and an explicit speciation profile of pyrogenic emissions. The model is driven by the Global Fire Emissions Database (GFED) version 1 or 2 for biomass burning, whereas biogenic emissions are provided either by the Global Emissions Inventory Activity (GEIA), or by a newly developed inventory based on the Model of Emissions of Gases and Aerosols from Nature (MEGAN) algorithms driven by meteorological fields from the European Centre for Medium-Range Weather Forecasts (ECMWF). The comparisons focus on tropical ecosystems, North America and China, which experience strong biogenic and biomass burning NMVOC emissions reflected in the enhanced measured HCHO columns. These comparisons aim at testing the ability of the model to reproduce the observed features of the HCHO distribution on the global scale and at providing a first assessment of the performance of the current emission inventories. The high correlation coefficients (r>0.8) between the observed and simulated columns over most regions indicate a very good consistency between the model, the implemented inventories and the HCHO dataset. The use of the MEGAN-ECMWF inventory improves the model/data agreement in almost all regions, but biases persist over parts of Africa and the Northern Australia. Although neither GFED version is consistent with the data over all regions, a better match is achieved over Indonesia and Southern Africa when GFEDv2 is used, but GFEDv1 succeeds better in getting the correct seasonal patterns and intensities of the fire episodes over the Amazon basin, as reflected by the higher correlations calculated in this region.

1 Introduction

Non-methane volatile organic compounds (NMVOCs) have a strong influence on tropospheric composition due to their impact on hydroxy radical (OH) levels and because of their contribution to ozone production in the presence of NO_x (Houweling et al., 1998). NMVOCs also influence the climate due to their role as precursors of secondary organic aerosols (SOA). Their lifetimes range from a few minutes to a few months. The largest source of NMVOCs is biogenic (1150 Tg C/yr, Guenther et al., 1995), as it represents about 85% of the total emission, the remainder being due to anthropogenic activities (12%, 161 Tg C/yr, Olivier et al., 2001) and vegetation fires (3%, 50 Tg C/yr, Andreae and Merlet, 2001; this study). Emissions of isoprene account for about half the total biogenic source (Guenther et al., 1995). However, due to their diversity, short lifetimes, and large spatiotemporal variability, the global burden as well as the speciation of NMVOCs are still highly uncertain.

Formaldehyde (HCHO) is the most abundant aldehyde in the atmosphere. A very small fraction is due to direct emissions by vegetation fires (Andreae and Merlet, 2001) and fossil fuel combustion (Olivier et al., 2003), but its main source is the chemical degradation of methane and the NMVOCs. Methane oxidation accounts for 60% of the global production of formaldehyde (ca. 1600 Tg/yr), the remainder being due to NMVOC oxidation, according to simulations performed using IMAGESv2, an updated version of the IMAGES global chemistry-transport model (Müller and Stavrakou, 2005). The contribution of directly emitted HCHO is small (<1% of the global total), yet it can be locally important, especially during fire events. Besides the relatively weak sinks associated with dry and wet deposition, the main sinks of HCHO include two photolysis reactions ($HCHO \rightarrow CO + H_2$ or $HCO + H$) and oxidation by OH ($HCHO + OH \rightarrow HCO + H_2O$). Although the reaction pathways leading from methane to HCHO are well established (e.g., Brasseur et al., 1999), the degradation mechanisms of the many NMVOCs are still very uncertain. For example, the globally averaged yield of HCHO from isoprene calculated using the MOZART model (Pfister et al., 2008) ($0.22 C^{-1}$, or 1.1 HCHO per

isoprene oxidized) is more than a factor of two lower than both the high NO_x and low NO_x yields (0.52 and 0.49C^{-1}) estimated using the Master Chemical Mechanism version 3 (MCMv3) (Saunders et al., 2003) (see also Sect. 4.2). The final yield of HCHO in the oxidation of isoprene under high NO_x conditions is about 20% higher in the MCMv3 (Saunders et al., 2003) than in the chemical mechanism of the GEOS-Chem model (Palmer et al., 2006). For monoterpenes and sesquiterpenes, uncertainties are even larger. For example the HCHO yield in the OH-initiated degradation of α-pinene, is equal to 0.31 per unit carbon in the MCM mechanism (Palmer et al., 2006), but it is estimated to be about 20 times lower according to recent theoretical studies (Peeters et al., 2001; Vereecken et al., 2007). In addition, large uncertainties are associated with the impact of isoprene on the oxidizing capacity of the atmosphere. Comparisons between the observations from recent tropical forest aircraft studies (Kuhn et al., 2007; Karl et al., 2007) and current models show that OH is largely underestimated in the boundary layer over the Amazon basin, possibly due to missing pathways or inaccurate reaction rates in the degradation mechanism of isoprene (Lelieveld et al., 2008).

Past studies have demonstrated the usefulness of HCHO column measurements from satellites as constraints on NMVOC emissions. GOME columns (Chance et al., 2000) have been used together with the GEOS-Chem model in order to investigate isoprene emissions over North America (Abbot et al., 2003; Palmer et al., 2006), at the global scale (Shim et al., 2005), in southeast Asia (Fu et al., 2007), and in South America (Palmer et al., 2007). Moreover, HCHO retrievals from the Ozone Monitoring Instrument (OMI) have been used to derive isoprene emissions over North America (Millet et al., 2008). Although these model studies demonstrate an excellent consistency between model results and satellite observations over several regions, like North America, serious discrepancies are often found in tropical regions, where the biomass burning and biogenic VOC source cannot be disaggregated. For instance, in spite of the large increases in the posterior isoprene (factor of 2–4) and biomass burning (factor of two) emissions over tropical Africa inferred by the inverse modelling study of Shim et al. (2005) for the period 1996–1997, a satisfactory agreement between the simulated

and the observed HCHO columns is not achieved after optimization.

In this article we present comparisons between the HCHO columns simulated with an updated version of the IMAGES CTM (Müller and Stavrakou, 2005) and a new dataset of spaceborne HCHO columns over the period 1997–2006. This 10-year record of HCHO columns retrieved from GOME and SCIAMACHY satellite instruments (De Smedt et al., 2008) is an air quality service of the Protocol Monitoring for the GMES Service Element: Atmosphere (PROMOTE) and Tropospheric Emission Monitoring Internet Service (TEMIS) projects (European Space Agency/Global Monitoring for Environment and Security-GMES) made available on the TEMIS website (www.temis.nl). It differs from previous retrievals (Chance et al., 2000; Wittrock et al., 2000, 2006) by the choice of the spectral window used, chosen to reduce artefacts over desert areas, minimize the noise, and produce a good degree of consistency between both instruments.

Our focus will be on tropical regions, where HCHO columns are dominated by pyrogenic and biogenic NMVOC emissions, as well as on North America and China, which experience enhanced biogenic emissions during the growing season. In order to provide meaningful comparisons of the model results with satellite data in regions where biomass burning is the dominant NMVOC source, the chemical scheme of the CTM has been extended and optimized with respect to HCHO production from pyrogenic NMVOCs. Due to the large uncertainties associated with pyrogenic and biogenic emission estimates, the model results are highly dependent on the emission inventories used in the comparisons. Two biomass burning inventories are tested in this study: the Global Fire Emission Database (GFED) version 1 (van der Werf et al., 2004), which has been extended until 2006 in the context of this study, and GFEDv2 (van der Werf et al., 2006). Both databases rely on fire counts detected from satellites, and cover the 1997 to 2006 period. Biogenic emissions are provided either by the GEIA database (Guenther et al., 1995), or by a new inventory (Müller et al., 2008), based on the MEGAN algorithm (Guenther et al., 2006). The 10-year comparisons between simulated and measured HCHO columns are intended as a means to test the ability of the model to reproduce the observed features of the formaldehyde distribution in different regions

of the world. These comparisons also provide a unique opportunity to assess the performance of emission inventories, highlight their potential strengths but also point to possible weaknesses.

This article is structured as follows. In Sect. 2 the satellite retrievals are briefly discussed. The pyrogenic and biogenic emission inventories are presented in Sect. 3. In Sect. 4 a detailed description of the proposed chemical mechanism is given, as well as the estimated contributions of individual NMVOCs to the total HCHO production. Section 5 is dedicated to the comparisons between modelled and observed HCHO columns over the eastern US, Tropical America, Africa, the Far East and Indonesia. Finally, the conclusions and the perspectives of this work are discussed in Sect. 6.

2 One decade of HCHO satellite columns

2.1 Slant column densities

Observations from two UV-visible nadir sounders, GOME (Global Ozone Monitoring Experiment) launched in April 1995 onboard the ERS-2 satellite (pixel size: $320\times40\,km^2$) and SCIAMACHY (Scanning Imaging Absorption Spectrometer for Atmospheric Chartography) launched in June 2001 onboard ENVISAT (pixel size: $60\times30\,km^2$), have been used to retrieve global tropospheric HCHO column densities by applying the differential optical absorption spectroscopy (DOAS) technique (Platt et al., 1994) in the near UV region. Both satellites are in sun-synchronous orbit with an equatorial local overpass time of 10:30 and 10:00, respectively.

Slant column abundances along the viewing path of the instruments are fitted within the 328.5–346 nm spectral window using a multi-purpose DOAS analysis software developed by Van Roozendael et al. (1999). This window is optimized to minimize noise, spectral interferences and artefacts over desert areas, and produces consistent HCHO datasets between GOME and SCIAMACHY observations (De Smedt et al., 2008). The HCHO absorption cross-sections applied in the DOAS fit are those of Cantrell et al.

(1990) convolved to the resolution of each instrument. The fitting procedure also includes reference spectra for interfering species (O_3, NO_2, BrO, and the O_2-O_2 collision). The Ring effect (Grainger and Ring, 1962) is corrected according to Chance and Spurr (1997) using solar irradiance measured by the satellite instrument as source spectrum. A linear intensity offset correction is further applied as well as a polynomial closure term of order 5. In order to avoid the GOME diffuser plate related artefacts (Richter and Wagner, 2001) and to reduce the residuals of the fit, Fraunhofer radiance spectra are selected on a daily basis in the equatorial Pacific Ocean, in a region where the HCHO concentration is low and mainly determined by methane oxidation. To further reduce the impact of zonally invariant artefacts, mainly due to unresolved spectral interferences with ozone and BrO absorptions, an absolute normalisation is applied on a daily basis using the reference sector method (see e.g. Khokhar et al., 2005), with the HCHO columns calculated by the IMAGESv2 model (see next section) in the reference Pacific sector.

2.2 Vertical column densities

The next step in the retrieval procedure is the calculation of the air mass factor (AMF) needed to convert the slant columns into the corresponding vertical columns. Because UV scattering by air molecules, clouds and aerosols makes the AMF sensitive to the vertical distribution of the absorbing molecule and to the surface albedo, air mass factors cannot be derived from straightforward geometric considerations, but instead require full multiple scattering calculations. If the trace gas, however, has a small absorption optical thickness, the scattering properties of the atmosphere can be separated from the vertical distribution of the absorber (Palmer et al., 2001), and the total air mass factor can be expressed as AMF$=\int w(h)S(h)dh$, where $w(h)$ are the scattering weights and $S(h)$ the shape factor.

The shape factor $S(h)$ is the normalised profile of the absorbing molecule. A priori HCHO profiles are provided by the IMAGESv2 model on a monthly basis and spatially interpolated at each satellite geolocation. The functions $w(h)$ represent the sen-

sitivity of the satellite measurements to the molecule concentration at each altitude and depend on the scattering properties of the observation. In this work, scattering weights have been evaluated from radiative transfer calculations performed with a pseudo-spherical version of the DISORT code (Stammes et al., 1988; Kylling et al., 1995). The scattering properties of the atmosphere have been modelled for a number of representative viewing geometries, UV-albedos and ground altitudes and stored in a look-up table. For each satellite observation, a sensitivity function is interpolated through this table.

A correction for cloud effects is applied based on the independant pixel approximation (Martin et al., 2001). Cloud fraction and cloud pressure are obtained from the Fast Retrieval Scheme for Cloud Observables (FRESCOv5) cloud product (Koelemeijer et al., 2002; Wang et al., 2008, http://www.temis.nl/fresco). The distribution of surface albedo is taken from the climatology of Koelemeijer et al. (2003).

No correction has been explicitly applied to account for the effect of aerosols on the air mass factors. The effect of non-absorbing aerosols is implicitly included through the cloud correction (Boersma et al., 2004), and results in a relatively small error (generally lower than 16%) on the air mass factor calculation. Absorbing aerosols can lead to a reduction of the air mass factor by up to 30–40% (Martin et al., 2003; Fu et al., 2007). The omission of the aerosol correction may thus significantly affect the derived HCHO column over fire scenes. The inclusion of an explicit aerosol correction in the retrieval algorithm will be addressed in future work.

Vertical tropospheric HCHO columns are derived by dividing the slant columns by the air mass factors. The columns used in this study include GOME data from 1997 to 2002 and SCIAMACHY data from 2003 to 2006.

2.3 Error estimation

Sources of errors in the retrieval of tropospheric HCHO columns include errors in slant column densities and errors in the evaluation of tropospheric air mass factors (De Smedt et al., 2008). For a single pixel, the random error on the slant columns of GOME,

expressed as the standard deviation of the measured columns around the mean, is estimated to increase from 4×10^{15} molec./cm^2 in 1997 up to 6×10^{15} molec./cm^2 in 2003, due to the instrumental degradation. For SCIAMACHY, the noise in the measurements is higher due to the shorter integration time, and the error on the slant columns reaches 1×10^{16} molec./cm^2. This error is reduced when the number of measurements increases. As a result, when averaging, this error term is divided by the square root of the number of satellite pixels taken into account in the mean.

An additional systematic error on the slant columns due to uncertainties in the slant columns cross-sections, interferences, non-linearities or inaccurate calibration has been considered. The most important error sources in the Tropics are parameters like the retrieval window and the HCHO absorption cross section, whereas at higher latitudes the ozone absorption and the Ring effect are dominant. The difference between the HCHO differential cross sections from the datasets by Cantrell et al. (1990) and Meller and Moortgat (2000) (12%) is taken as an estimate for the systematic error on this parameter. In addition, an estimated error of 12% on the slant columns is included to account for other sources of errors. The total systematic error ranges from 2.5×10^{15} molec./cm^2 in the Tropics to 8.0×10^{15} molec./cm^2 at high latitudes.

The error in the evaluation of the air mass factors is mainly due to uncertainties in vertical HCHO profiles, cloud effects and the ground albedo. For clear sky conditions, the total error on the AMFs is estimated at 18% with equal contributions from the albedo and the profile shape uncertainties. The error increases with cloud fraction, mainly for low altitude clouds, up to 50% for a cloud fraction of 0.5. In this work, monthly HCHO averages are calculated using observations with a cloud fraction below 0.4. The total uncertainty on the monthly HCHO vertical column generally ranges between 20 and 40%, depending on the observation conditions (De Smedt et al., 2008).

3 Model description

3.1 IMAGESv2 chemical transport model

The IMAGESv2 CTM is an updated version of the IMAGES model (Müller and Stavrakou, 2005). Recent updates and improvements are briefly discussed in this section. The model provides the global distribution of 20 short-lived and 48 long-lived (i.e. transported) chemical compounds between the Earth's surface and the pressure level of 45 hPa through a chemical mechanism comprising 164 gas-phase reactions, 39 photodissociations and 3 heterogeneous reactions on the surface of sulfate aerosols. The model is run at a horizontal resolution of 5 degrees and is discretized in the vertical on 40 hybrid sigma-pressure layers. Monthly mean ECMWF/ERA40 reanalysed wind fields (Uppala et al., 2005) from September 1996 to December 2001 and ECMWF operational analyses beyond this date drive the advection represented by a semi-Lagrangian scheme (Smolarkiewicz and Rasch, 1991). The surface pressure, temperature and humidity fields are also monthly averages derived from the same ECMWF analysis. Horizontal and vertical diffusion coefficients are estimated using the ECMWF wind variances. ERA40 updraft mass convective fluxes are used until 2001, whereas a climatological mean over 1995–2001 is used beyond this year. Turbulent mixing in the planetary boundary layer (PBL) is parameterized as vertical diffusion.

The model time step is equal to one day and the model calculates daily averaged concentrations. Correction factors are applied on the photorates and the chemical kinetic rates to account for diurnal variations in the photorates and in the concentrations. They are given by $\gamma_i = \frac{<k_i C_A C_B>}{<k_i><C_A><C_B>}$, C_A and C_B being the concentrations of the reactants A and B, k_i the rate of the reaction i, and <> the 24-h mean. The correction factor calculation is performed off-line from full diurnal cycle calculations using diurnally varying photorates and emissions with a 20-min time step using the fourth order Rosenbrock solver of the KPP package (Damian et al., 2002; Sandu and Sander, 2006). The HCHO diurnal profiles calculated from this simulation are also used to es-

timate the HCHO concentration at the satellite overpass time from the daily averaged values calculated with one day time step.

The calculated columns are evaluated against HCHO observations between January 1997 and December 2006, following a 4-month spin-up time. Archived fields from previous simulations are used as initial conditions.

Anthropogenic CO and total NMVOC emissions are taken from the EDGAR v3.3 inventory for 1997 (Olivier et al., 2001, Olivier, 2002, see also http://www.mnp.nl/edgar/). Speciation of VOC emissions is obtained from the POET database (Olivier et al., 2003), except for biofuel emissions where we use the updated speciation by M. O. Andreae (personal communication, 2007) (Andreae and Merlet, 2001).

3.2 Pyrogenic emission inventories

The distributions of vegetation fires are provided by the Global Fire Emissions Database (GFED) version 1 (van der Werf et al., 2004) and version 2 (van der Werf et al. (2006) for the period from 1997 to 2006. These databases combine information on burned area for selected regions (Giglio et al., 2006) with fire hot spot data (Giglio et al., 2003; Justice et al., 2002), and biogeochemical modelling to estimate carbon emissions (van der Werf et al., 2003). Emission factors provided by Andreae and Merlet (2001) with updates from M.O. Andreae (personal communication, 2007) have been used to derive trace gas emissions from the carbon emissions. A total number of 16 explicit NMVOCs are pyrogenically emitted in the current version of the model, whereas a lumped species accounts for the emissions of the non-explicit NMVOCs, as discussed in Sect. 4.

The GFEDv1, released in 2004, is based on a single relation between burned area from 16 MODIS "tiles", each covering an area of 10×10 degrees, and TRMM-VIRS fire hot spots. This relation is dependent on the tree cover fraction; in general, one hot spot represents more burned area in grassland than in forests due to the faster spread rate in grassland, and thus the smaller probability of detection (van der Werf et al., 2003).

Burned area reprocessing and refinements to the biogeochemical model, resulted in

a new version of GFED, released in 2006 (GFEDv2). The main differences with the first version stem from the use of MODIS hot spots, a much larger number of burned area tiles that are processed (446), a regional fire hot spot to burned area relation (Giglio et al., 2006), the inclusion of combustion of belowground carbon, and the use of fire persistence to increase combustion completeness due to multiple ignitions in deforestation regions. The large number of tiles allows for a regional fire hot spot/burned area model to account for regional variations in the use of fire. The model uses also herbaceous vegetation cover, the mean size of monthly cumulative fire-pixel clusters size, and regression trees in order to derive the fire hot spot/burned area relation (Giglio et al., 2006). More specifically, in GFEDv1 only above ground biomass can burn. However, especially in the boreal regions and Indonesia, below ground carbon also burns. Regionally this source may be more important than the combustion of above ground biomass. Another modification is based on fire persistence; in areas undergoing deforestation, fuels are often ignited multiple times to enhance the combustion completeness. This translates into several fire observations over a period of weeks to months within one location. Where this is observed, the combustion completeness is increased in GFEDv2.

Zonally and monthly averaged NMVOC emissions derived from the GFEDv1 and GFEDv2 databases are displayed in Figs.1 and 2, respectively, as well as their annual global estimate. The average global NMVOC emissions amount to 109 Tg/yr and 96 Tg/yr according to GFEDv1 and GFEDv2, respectively. In general, version 2 has lower overall emissions (due to lower burned area) but higher interannual variability (as this variability stems mostly from fires in deforestation regions and areas where belowground carbon burning is important), and the peak fire season is delayed by a month in the Southern Hemisphere (due to the use of MODIS fire spots instead of those derived from TRMM). The highest NMVOC emissions occur during the El Niño years 1997–1998, whereas the lowest values occur in 2000/2001 for the GFEDv2 and in 2006 for the GFEDv1 database.

The diurnal profile of biomass burning emissions displayed in Fig. 3 is applied in the

diurnal cycle calculations with the CTM. This profile is based on fire observations from satellites over 15 tropical and subtropical regions (Giglio, 2007). The diurnal distribution of fire activity has a maximum in the afternoon, little or no burning during the night and in the early morning, and a slightly longer tail behind the afternoon peak.

To account for fire-induced convection, the biomass burning emissions are distributed over six layers from the surface to 6 km (0–100 m, 100–500 m, 500–1 km, 1–2 km, 2–3 km, 3–6 km), according to the spatially-dependent fractional distribution of emission heights provided in Dentener et al. (2006).

3.3 Biogenic emission inventories

Biogenic emissions of isoprene are calculated using the MEGAN model (Guenther et al., 2006) coupled with the MOHYCAN canopy environment model (Wallens, 2004; Müller et al., 2008). The emissions are calculated off-line at a high spatial (0.5° × 0.5°) and temporal (hourly) resolution, and then regridded at the resolution of the IMAGESv2 model (5° × 5°, daily). Monoterpene emissions are neglected. The isoprene emission rate E at a specific location and time is expressed as

$$E = 0.52 \cdot \epsilon \cdot \left(\sum_k (\gamma_P)_k \cdot (\gamma_T)_k \cdot (\mathrm{LAI})_k \right) \cdot \gamma_{\mathrm{age}} \cdot \gamma_{\mathrm{SM}}, \quad (1)$$

where ϵ (mg m^{-2}h^{-1}) represents the emission at standardized conditions defined in Guenther et al. (2006). The factor 0.52 is necessary to ensure that $E = \epsilon$ for these standard conditions. The response to the photosynthetic photon flux density (PPFD, μmol m^{-2}s^{-1}) and the leaf temperature is taken into account by γ_P and γ_T emission activity factors (Guenther et al., 2006), respectively. LAI is the leaf area index. The sum is considered over the layers of the canopy model, which provides the incident PPFD and temperature of sun and shade leaves at each of the depths of the modelled canopy, and is driven by values at the canopy top of PPFD and near infrared radiation flux, relative humidity, air temperature, and windspeed (Müller et al., 2008). The factor γ_{age}, representing the dependence on the leaf growth state for deciduous canopies, is

parameterized from LAI changes between current and previous time steps (Guenther et al., 2006). The factor γ_{SM} accounts for the emission response to soil moisture stress. The total emission for a given location is expressed as the sum of the emissions calculated for all the plant functional types present in the given model grid cell, for clear sky and cloudy conditions.

We drive MEGAN with ECMWF fields for the downward solar flux, the cloud cover fraction, as well as for the air temperature, dewpoint temperature, and windspeed directly above the canopy. Reanalysed ERA40 fields are used until 2001 and operational analyses are used beyond this date. Monthly mean LAI values derived from the MODIS satellite instrument (Zhang et al., 2004) from 2001 onwards are used, and a climatological mean over 2001–2006 is used before this date. The landcover is taken from Guenther et al. (2006). The soil moisture is provided by the ECMWF/ERA40 model analyses, and the soil moisture at the permanent wilting point is taken to the value used in the ECMWF model (0.171 $m^3 m^{-3}$).

We determine the PPFD under clear sky conditions by using a radiative transfer model (Madronich and Flocke, 1998), and the ratio of the PPFD to the total solar radiation from the ISCCP dataset (Rossow et al., 1996, http://isccp.giss.nasa.gov/). Using the cloud cover fraction and the total solar radiation flux, the cloud optical depth is determined, and thereby, the PPFD in cloudy conditions. The PPFD and near infrared fluxes for cloudy and non-cloudy skies are used as input in the canopy model. A thorough description of the emission inventory can be found in Müller et al. (2008) and the monthly averaged emissions (in mg isoprene /m^2/hr) at a resolution of 0.5 degree are available in NetCDF format at the www.aeronomie.be/tropo/models/mohycan.htm website.

The emissions are daily averaged and gridded onto the resolution of IMAGESv2. Globally, the MEGAN-ECMWF annual estimates are about 30% lower than the standard MEGAN estimate (Guenther et al., 2006). The difference is mainly due to the impact of the soil moisture stress factor which is found to decrease the global emission estimates by more than 20% (Müller et al., 2008). The GEIA database (Guenther

et al., 1995) is used in this study as an alternative prior inventory. The differences between the GEIA and the MEGAN-ECMWF databases are mainly related to the emission algorithms used. The MEGAN model is based on an extensive compilation of field measurements, and includes the dependencies of the emission on the leaf age and on the soil moisture stress factor. In addition to this, the emissions of the MEGAN-based inventory account for the diurnal, daily, seasonal and year-to-year variability, while the GEIA inventory provides one emission field per month without accounting for the interannual variability due to the changing meteorology.

The biogenic source of methanol is calculated as in Jacob et al. (2005), and amounts to 130 Tg/yr due to the plant growth process and 22 Tg/yr due to decaying dead plant matter. Biogenic emissions for CO, NO_x and other NMVOCs are described in Müller and Stavrakou (2005), as well as ocean emissions of CO and NMVOCs.

4 Optimization of the chemical scheme with respect to HCHO production

4.1 The chemical scheme

The NMVOC chemistry species, chemical reactions and kinetic rates are presented in the supplement http://www.atmos-chem-phys-discuss.net/8/16981/2008/acpd-8-16981-2008-supplement.pdf. The inorganic chemistry reactions, as well as the methane degradation mechanism, are kept the same as in Müller and Stavrakou (2005), with updated kinetic rates from Sander et al. (2006).

The degradation mechanism for the majority of the NMVOCs is largely based on the Master Chemical Mechanism (MCM) (Saunders et al., 2003). For isoprene, the condensed Mainz Isoprene Mechanism (MIM) (Pöschl et al., 2000), derived from the MCM, has been adopted with some modifications. More precisely, the mechanism includes compounds that do not appear explicitly in the MIM, like glycolaldehyde and glyoxal. The oxidation of isoprene hydroxynitrates by OH is adapted directly from the MCM, with the product NO_2 being replaced by HNO_3, a more likely product in the OH-

addition pathway of alkylnitrates (Atkinson, 1994). Further, the rate constant for the formation of methacrylic peroxynitrate (MPAN) is multiplied by a factor of 0.12, i.e. the yield of acylperoxy radicals in C_5H_8+OH according to the MCM (0.27) multiplied by the ratio of the NO-reaction rates of alkylperoxy and acylperoxy radicals (0.43).

4.2 HCHO Yields From NMVOC Oxidation

We present here calculations of the HCHO yields from the oxidation of different NMVOCs using the fully explicit Master Chemical Mechanism v3.1 (Saunders et al., 2003), and we compare with the HCHO yields calculated with the IMAGESv2 chemical mechanism (Table 1). To allow a meaningful comparison between the HCHO yields calculated with two different mechanisms, we employ in IMAGESv2 the same inorganic chemistry and photolysis rates provided for the MCM, except for the quantum yield of hydroxyacetone, which is taken equal to that of acetone and for the quantum yield of methacrolein (MACR) and methyl vinyl ketone (MVK) which follow the recommendation of Sander et al. (2006).

Box model time-dependent simulations have been performed in both cases using the chemical solver of the KPP package. Simulations start at 06:00 for a temperature of 298 K at a latitude of 30 degrees in February. The model is initialized with 0.1 ppb of the considered NMVOC, 35 ppb O_3, and 100 ppb CO. The NO_2 concentration is kept constant throughout the simulations and is taken equal to 1 ppb; such a choice reflects the high NO_x regime associated to biomass burning events. Simulation results using 0.1 ppb NO_2 have been also obtained, but are generally omitted in the discussion below, except for the important case of isoprene, a compound emitted in both high NO_x and low NO_x environments.

Two HCHO yields are computed: after one day of simulation (short-term yield), and after 2 months ("ultimate" or final yield). The short-term yield is defined as

$$Y_{st} = (\text{HCHO produced after 1 day})/C_0(\text{NMVOC}), \quad (2)$$

where C_0(NMVOC) is the initial concentration of the NMVOC. This yield represents the

ACPD
8, 16981–17036, 2008

number of HCHO molecules generated by a given NMVOC one day after the injection time. The short-term yield defined in Eq. (2) provides better indication of the HCHO production that may be detected by the satellite instrument directly above biomass burning areas. The final yield is defined as

$$Y_f = (\text{HCHO produced})/\Delta C(\text{NMVOC}), \quad (3)$$

where ΔC(NMVOC) is the difference between the initial and the final NMVOC concentrations. Due to the importance of both short-term and final yields in the correct representation of the HCHO production by our chemical mechanism, particular care has been taken to ensure that the IMAGESv2 calculated HCHO yields are as close as possible to the MCM yields, as is evident from Table 1.

Ethene has the highest short-term HCHO yield per unit carbon (0.7), followed by propene (0.6), 2,3-butanedione (0.5), acetaldehyde (0.47), and isoprene (0.46). Strongly emitted compounds like acetic acid and methanol with lifetimes of several days have very small 1-day yields. For relatively short-lived species like ethene, glycolaldehyde, propene, acetaldehyde, and isoprene, more than 80% of the final yield is reached within the first day in the box model simulations. The shortest-lived compounds glyoxal, methylglyoxal and biacetyl reach their ultimate HCHO yield within only a few hours.

Both IMAGESv2 and MCM yields of HCHO from isoprene are about 20% higher than the yield calculated with the GEOS-Chem mechanism (Evans et al., 2003) under high NO_x conditions (Palmer et al., 2006). The GEOS-Chem yield has been found by Millet et al. (2006) to be consistent with aircraft measurements of isoprene and formaldehyde over North America. The molar primary yields of MVK (0.33), MACR (0.23) and HCHO (0.6) estimated from laboratory studies (Atkinson et al., 2006) are well reproduced by the MCM, except for a slight overestimation concerning HCHO (yields of 0.34, 0.22 and 0.67, respectively). The formation of HCHO observed in MVK and MACR photooxidation experiments has also been shown to be fairly well reproduced by the MCM mechanism (Pinho et al., 2005), when replacing the strongly overestimated quantum yields of MVK and MACR of the MCMv3

by values in line with the recommendations of Sander et al. (2006) adopted in IMAGESv2 (see supplement http://www.atmos-chem-phys-discuss.net/8/16981/2008/acpd-8-16981-2008-supplement.pdf). In conclusion, the HCHO yield from isoprene at high NO_x appears to be only slightly biased in the IMAGESv2 mechanism according to the available laboratory data. The yield dependence on the abundance of NO_x is more uncertain. As illustrated in Table 2, both MCM and IMAGESv2 are only slightly lower at low NO_x (0.1 ppbv NO_2) compared to high NO_x (1 ppbv) (by 10% and 16% in MCM and IMAGESv2, respectively). This contrasts with the stronger dependence found in the GEOS-Chem mechanism, with 35%–50% lower yields under low NO_x levels, due to the loss of carbon in lumped products of organic hydroperoxide reactions in this mechanism (Palmer et al., 2006).

The MCM-computed HCHO yields from α- and β-pinene under the aforementioned conditions are 0.2 and 0.17, respectively (see also Palmer et al., 2006). However, the primary yield of HCHO from α-pinene+OH is estimated to be lower than 0.02 C^{-1} according to theoretical estimates and in agreement with laboratory data (Peeters et al., 2001 and references therein). Therefore, despite the fact that biogenic emissions of terpenes can exceed those of isoprene for some ecosystems, terpenes are thought to contribute little to the HCHO columns, and will be omitted from the present analysis.

4.3 Quantifying the HCHO production from vegetation fires

The HCHO production by a NMVOC is calculated as

$$P(HCHO) = P(NMVOC) \cdot Y \cdot MW_{HCHO}/MW_{NMVOC},$$

where P(NMVOC) is the pyrogenically emitted NMVOC, MW its molecular weight, and Y the short- or long-term yields computed by the MCM or the IMAGESv2, as shown in Table 1 and described in Sect. 4.2.

The total ultimate HCHO production from fires is estimated at about 63 Tg/yr, half of which is produced after one day. As illustrated in Table 1, only three NMVOCs, namely acetic acid, methanol and ethene, account for one third of the total short-term HCHO

production, and 43% of the final production. Among them, the oxidation of ethene contributes the most, 27% in the short-term and 18% in the long-term HCHO production, whereas the slowly reacting methanol and acetic acid, contribute mainly to the final production term. Other important contributions to the short-term HCHO production come from directly emitted HCHO (14%), C_3H_6 (12%), 2,3-butanedione (7%), and CH_3CHO (6%). Glyoxal, although abundantly emitted during fire events, leads to a negligible HCHO formation. Insignificant is also the impact of aromatic NMVOCs (benzene, toluene and xylenes) to the total HCHO production (1–2%), and therefore these compounds are not included explicitly in the present study. Although formic acid, hydrogen cyanide and acetonitrile represent about 9% of the total NMVOC emissions, they do not lead to HCHO formation after oxidation. The compounds explicitly included in the IMAGESv2 chemical mechanism represent about 87% of the total short- and long-term HCHO production, the remainder being accounted for by the surrogate species C_4H_{10} (Müller and Stavrakou, 2005).

Since the short-term and final HCHO productions given in Table 1 have been calculated under high NO_x conditions, and neglecting wet and dry deposition losses of oxygenated intermediates, they should be seen as only an upper limit of the HCHO produced in the atmosphere.

5 Simulated vs. observed columns

5.1 Contribution of the different emission sources to the total HCHO column

The aim here is to calculate the contribution of different emission sources to the total annual modelled HCHO columns. Model runs are conducted for the year 2006 using the GFEDv2 biomass burning inventory and the MEGAN-ECMWF isoprene database.

To sidestep the feedbacks of the emissions on the oxidants concentrations, we archive monthly OH, HO_2, NO, NO_2 and NO_3 fields from a full simulation with all sources included. The contribution of each source category to the total HCHO column

is calculated by including only emissions from that source, while keeping the concentrations of the oxidants at the archived values throughout the simulations. The four categories considered are the oxidation of methane (together with a small oceanic NMVOC source), anthropogenic emissions, vegetation fires and biogenic emissions. The resulting annual mean HCHO columns are shown in Fig. 4, as well as the global amount of HCHO produced annually by the corresponding source. As illustrated in this figure, the oxidation of methane in the background troposphere represents 60% of the HCHO source on the global scale (HCHO yield from methane oxidation is equal to ca. 0.9). However, oxidation of locally emitted NMVOCs generally dominates over continents. Among the NMVOCs, biogenic compounds (mostly isoprene) are dominant and contribute up to 30% on the global scale. Although anthropogenic sources are significant in populated and industrialized areas, they are responsible for only 7% of the total source. The smallest contribution (3%) comes from biomass burning. Although insignificant on the global scale, fire episodes lead to locally enhanced HCHO columns detectable by the satellites, especially in tropical regions.

A comparison between the annually averaged spaceborne HCHO columns and the corresponding simulated columns is presented in Fig. 5 for 1997 and 2005. Regions with enhanced HCHO concentrations are clearly mostly related to biogenic emissions and biomass burning. The model reproduces well the observed distribution over continental regions and to some extent over the oceans, in particular below the Tropics. The SCIAMACHY columns tend to be slightly larger than both the modelled and the GOME values, especially at mid-latitudes of both hemispheres. As already discussed by De Smedt et al. (2008), the offset found between GOME and SCIAMACHY columns generally increases with latitude, and concerns primarily the winter values. Still, even for Europe, the offset (1.3×10^{15} molec.cm^{-2}) is largely below the estimated errors on the vertical columns. Over the eastern US, the offset appears to be negligible during summertime.

The seasonal variability of the monthly averaged observed and modelled columns for the year 2000 is illustrated in Fig. 6. The averages from the model account for the sam-

pling times of observations at each location. The model generally reproduces well the seasonal variation of the HCHO columns over the main emission regions (continental Tropics, US and China), which are the main focus of our study. Noticeable exceptions (e.g. over Southern Africa in September–October, see Fig. 6) can be generally attributed to the emissions used in the model, as will be discussed in detail later.

5.2 Performed simulations

Three 10-year model simulations are conducted, using different combinations of emission inventories, as summarized in Table 3. The modelled HCHO columns in each of these simulations are evaluated against observed columns over the individual model grid cells and regions displayed in Fig. 7. Given the high noise and poor agreement between the model and the observations at high latitudes (e.g. Europe, Canada, and Siberia) and in the region influenced by the South Atlantic Anomaly (South America around 30° S), these areas will be excluded from the discussion. Furthermore, since the chemical scheme used in the model is not optimized with respect to HCHO production from anthropogenic NMVOCs, our interest focuses mainly on the Tropics, where pyrogenically and biogenically emitted NMVOCs are primarily responsible for the enhanced HCHO abundances (Figs. 4, 5), the anthropogenic contribution being much less important (Fig. 4). Comparisons are also provided over eastern US and China since the HCHO columns are still dominated by the biogenic source, being about twice as large as the anthropogenic source strength, as shown on the 2006 annual mean of Fig. 4.

5.3 Eastern US

In Fig. 8, the monthly averaged modelled columns are confronted to observed HCHO columns over the eastern United States (regions 1 and 2 of Fig. 7). Black, green and red solid lines correspond respectively to the S1, S2 and S3 model simulations described in Table 3. The strong seasonal variation in the observed HCHO columns over

this region, with values about a factor of two higher in summer than in winter, correlates clearly with the growing season characterized by enhanced isoprene emissions, as already reported in Abbot et al. (2003) and Palmer et al. (2006). Both biogenic emission datasets are in good consistency over this region and capture the seasonal variations very well. This is reflected in the very high correlation between the modelled and the observed columns ($r \sim 0.90$), even though the model is biased high by 15–30% on average in summertime. This overestimation contrasts with the underestimation of GEOS-Chem HCHO compared to the Harvard GOME columns (Chance et al., 2000) over eastern US by 20–30% (Palmer et al., 2006). Part of the overestimation in our study could be due to the relatively high yield of formaldehyde from isoprene in our chemical mechanism, as discussed in Sect. 4.2. More importantly, the GOME HCHO columns used in this work are by about 30% lower in this region than the Harvard GOME columns (De Smedt et al., 2008), which have been found to be up to 14% higher than OMI HCHO columns in the eastern US (Millet et al., 2008). The reasons for these discrepancies are currently unknown. A detailed intercomparison between the datasets is clearly needed to cast light upon the causes of these differences.

The red dashed curve in Fig. 8 represents the result of a sensitivity calculation where isoprene emissions have been halved over North America. Reduced emissions lead to a reduction of the model/data bias for all years, the improvement being more significant over the southeastern US.

The ability of the model to reproduce independent HCHO observations over this region is tested in Fig. 9, where the IMAGESv2 profiles derived from the S2 simulation and from the simulation with the reduced biogenic source are compared with the mean observed vertical distribution during the INTEX-A campaign (July–August 2004, Singh et al., 2006) over four regions. The measurements were performed by two groups, the National Center for Atmospheric Research (NCAR) and the University of Rhode Island (URI) and are publicly available at the NASA data center website (http://www-air.larc.nasa.gov/). Different measurement methods were used by the two groups, namely, tunable diode laser absorption spectrometry (Fried et al., 2008) by

NCAR and an automated coil enzyme fluorometric system by URI (Heikes et al., 2001). The URI dataset has systematically lower values than the NCAR data, by about 30% in the boundary layer. The S2 modelled mixing ratios (black lines in Fig. 9) at altitudes higher than 1.5 km lie mostly between the values defined by the two datasets, whereas over the continental boundary layer they are more than 10% higher than the NCAR masurements, and by about 20% higher than in the GEOS-Chem CTM (Millet et al., 2006). Over the ocean, the agreement is very good between our values, GEOS-Chem and the observed mixing ratios. Reducing the biogenic source by a factor of two results in a 20–25% decrease of the HCHO concentration in the boundary layer, which is now found to lie always in between the values provided by the two datasets. This finding can be considered as an indirect validation of the spaceborne HCHO dataset used in this study.

Note finally that the biogenic source estimate of the MEGAN-ECMWF inventory over the Northern US is in excellent consistency with the estimation by Palmer et al. (2006) based on a slightly different version of MEGAN using NCEP data, i.e. the MEGAN-ECMWF emissions are about 10% lower than in the GEIA inventory (Guenther et al., 1995), when the soil moisture stress is not accounted for, as in the calculation in Palmer et al. (2006).

5.4 Tropical America

Comparisons are shown on Figs.10 and 11 over several regions of Central and South America. The modelled columns correlate well with data over these regions (r>0.7), except for the Brazil Nordeste (r=0.58–0.68). The high correlation coefficient values (~0.9) calculated over the extended Amazonian region, Guatemala and Santarem yield strong confidence to the spatiotemporal distribution of the implemented emission inventories. Important reductions of the model/data discrepancies in most of the regions are achieved when the lower emissions of the MEGAN-ECMWF inventory are used, as illustrated in Fig. 11.

Although once rarely touched by fires, the Amazon rainforest now experiences

human-induced fires, which render the damages caused by natural droughts, related principally to the El Niño events, even more devastating. The Amazonian drought in 1997/1998, caused by the exceptionally strong El Niño event, and the 2005 extended dry season, most probably associated with the atlantic multidecadal oscillation (Marengo et al., 2008), resulted in increased fire activity (Aragão et al., 2007). The HCHO column enhancements caused by these fires are quite well captured by both GFEDv1 and 2 (Figs. 1,2), although their magnitude and timing may differ. The main burning season spans August through October over the Amazonia basin, as illustrated in Figs. 10 and 11. As seen on these figures, the S2 simulation using GFEDv1 allows for a better match with the measurements compared to the S3 model run in most of the selected regions.

Over the extended Amazonian region, the higher fire emissions of GFEDv1 and the lower values of the MEGAN-ECMWF emissions (S2 run) provide an excellent consistency with the measured columns (correlation coefficient of 0.91), which contrasts with previously conducted studies (Shim et al., 2005). The agreement is very good over the Guatemala grid cell in both (wet and dry) seasons. Over Northern Peru, while the use of GEIA inventory leads to systematically overestimated columns (by up to 50%), a substantial bias reduction is achieved when using the lower emissions of the MEGAN-ECMWF inventory. The GFEDv2 succeeds well in capturing the dry season maxima over the Peru-Bolivia-Brazil grid cell, but fails in getting the right magnitude over N-E Brazil and Santarem. A strong correlation is also found between measured and modelled columns over the Santarem region. It should be noted, however, that the MEGAN-ECMWF isoprene fluxes are found to be largely overestimated, especially in the wet season, when compared to surface flux measurements conducted at the Tapajós National Forest (2°51′ S, 54°58′ W), although the adequacy of a comparison between averages over a large region and point measurements can be questioned (Müller et al., 2008). The seasonal pattern of these flux measurements is in agreement with in-situ isoprene concentration measurements for 2002 (Trostdorf et al., 2004). Further measurements are obviously needed in order to assess the representativity of these

measurements at a larger scale.

5.5 Africa

Over Africa, North of the equator, the dry season extends from November through March, and the rainy season from April through October, whereas in the Southern Hemisphere the contrary is true. On both sides of the equator, however, local climates with two dry and two wet seasons are found. The two biomass burning inventories capture reasonably well the timing of the fires, yet several differences exist regarding the intensity of the maxima as well as the seasonal patterns. The correlation coefficients between the simulated and observed columns are found to be significantly higher when the MEGAN-ECMWF inventory is used in three of the four regions shown in Fig. 12.

Over the Central African Republic, a satisfactory agreement with the observations is obtained with GFEDv1, whereas systematically overestimated columns, especially in January (up to 100% in 2000/2001) are derived when GFEDv2 is used. The wet season over this region is characterized by significantly lower emissions compared to the dry season (factor of two). The higher values of the MEGAN-ECMWF biogenic emissions lead to a reduction of the model/data bias for most of the years.

Over Southern Africa, the use of the MEGAN-ECMWF emissions increases the correlation between modelled and observed columns by 36% (from 0.44 to 0.6) compared to the simulation using the GEIA inventory. Nevertheless, it results in a general underestimation (up to 20%) of the modelled columns, except during the dry season, when hydrocarbon emissions by fires dominate over the biogenic source. This could be possibly due to a bias in the retrievals and/or to an underestimation of biogenic emissions over this region. In fact, field studies characterizing species composition and isoprene emission factors conducted over this region allowed for the determination of the MEGAN isoprene emission estimates with less uncertainties than those for many other regions (Otter et al., 2003). On the other hand, the low emission rates of the MEGAN-ECMWF inventory used in the CTM simulations might be partly due to the soil moisture stress (Müller et al., 2008), which could have influenced the campaign

measurements at the Southern African locations used to determine the MEGAN basal emission rates (Guenther et al., 2006). It is more likely, however, that the very simple parameterization for soil moisture stress used in MEGAN might not be appropriate (except for shutting off emissions in severe drought conditions). During the dry season, the one-month delay in the fire peak in the GFEDv2 is supported by the observations and results in a higher correlation coefficient (0.71), compared to the simulation using the GFEDv1 (0.6). The GFEDv1 maximum of June 2000, not supported by the observed HCHO columns which peak in July, was also found to lead to an overestimation of simulated CO columns in an inverse modelling study using the MOPITT CO data as top-down constraints (Stavrakou and Müller, 2006).

Over the Ivory coast region, the use of the GFEDv2 results in generally underestimated columns during the fire season, whereas the emission peaks and their variations are better captured in the S2 simulation. Both biogenic inventories are in good agreement, although the higher GEIA values improve generally the agreement with the data. However, there are no isoprene emission measurements reported for this region, and the MEGAN-ECMWF estimates are expected to be highly uncertain. In the equatorial rainforest of Congo, which experiences two dry seasons and two wet seasons every year, the use of the MEGAN-ECMWF inventory leads generally to lower modelled HCHO columns, but with a seasonal variation closer to that of the observations. The biogenic emission estimates for Congo derived by MEGAN are based on a limited set of aircraft or tower flux measurements that indicate that this region has generally low isoprene emissions. Both biomass burning inventories, however, miss the observed maximum in February.

5.6 Asia and Australia

The use of MEGAN-ECMWF isoprene emissions improves the agreement with the data in all regions of Figs.13 and 14, especially over northern Australia, where the correlation coefficient between modelled and observed columns is increased from 0.32 to 0.74. A further increase of the correlation is achieved in most regions when using

GFEDv2 instead of GFEDv1 (0.80 in northern Australia).

The monthly mean HCHO columns over Northern and Southern China (Fig. 13) exhibit a pronounced seasonal cycle associated to enhanced biogenic emissions. The modelled columns using the GEIA inventory (black line) are overestimated by up to 20–40% in the growing season (May–October), whereas the use of the lower MEGAN-ECMWF emissions (S3 simulation) leads to a better agreement over both regions. The slight underestimation showing up after 2002 can be partially explained by a small offset between the GOME and SCIAMACHY column data (De Smedt et al., 2008). Another possible explanation could be a positive trend of isoprene emissions in China, especially over small spatial scales, due to massive afforestation programs which rank China as the country with the highest recorded annual planting rates (Geron et al., 2006). Such changes however, should happen progressively throughout the years, as tree plantations become mature and emit isoprene at higher rates (Guenther et al., 2006). Both pyrogenic inventories agree on their estimates of burnt biomass over China and provide a satisfactory agreement with the observations, except in April 2002 where neither inventory succeeds in capturing the elevated HCHO value.

Total biomass burning NMVOC emission from GFEDv2 for Far East and South Asia is estimated to about 20 Tg/yr for 1997–2001 average fire activity, and to 5.5 Tg for the year 2000, a factor two lower than the prior estimate (12 Tg) used in the inversion study of Fu et al. (2007) for the same year. Their inversion constrained by GOME HCHO columns (Chance et al., 2000) suggests a five-fold increase of the biomass burning source, which is not supported by out comparisons. Further, the MEGAN-ECMWF biogenic fluxes averaged over the 1997–2001 period are by 40% lower that the GEIA source (62 vs. 87 Tg/yr), but agree reasonably well with the posterior estimate of Fu et al. (2007) (56 Tg/yr).

The extremely high values of the monthly mean HCHO columns over Indonesia in September/October 1997 (up to 2.5×10^{16} molec./cm^2) are due to the El Niño-induced fires, which raised the pollution levels to unrecorded heights over Sumatra and Borneo. This peak is overestimated by the model by a factor of two over Borneo when GFEDv2

is used, but this simulation correlates better with the data (r=0.98) than the simulation with GFEDv1 (r=0.94) in 1997. Below ground burning, taken into account in GFEDv2, leads to enhanced fire emissions over Indonesia, and is the main reason for the discrepancy between the two inventories over these regions. The inclusion of peat fires in the GFEDv2 is partly supported by our comparisons, because of the better correlation with the data, even though modelled columns are biased high in some years.

Over Northern Australia, the use of the MEGAN-ECMWF inventory leads to a large overestimation (by up to 50%) of HCHO columns relative to the satellite observations. Over this continent, woody vegetation is dominated by *Eucalyptus* trees. The very high isoprene emission estimated for Northern Australia by MEGAN-ECMWF is primarily based on the assumption that all *Eucalyptus* trees emit isoprene. Although high isoprene emission rates have been reported for several *Eucalyptus* species (He et al., 2000), this represents only a few percent of the more than 700 Eucalyptus species found in Australia (Cronin, 2000). In addition, since it is known that other diverse genera, including oaks and acacias, have both isoprene emitters and non-emitters, it would not be unreasonable to suppose that at least some eucalypts emit small or negligible isoprene quantities. Measurements on the dominant Australian species are necessary to determine whether the assumptions made in the MEGAN model lead to overestimated isoprene emissions in northern Australia. The use of MEGAN-ECMWF inventory, however, improves considerably the agreement regarding the seasonal variation of the observed HCHO columns, since the biogenic emissions over this region show a strong seasonality (Müller et al., 2008).

6 Conclusions

A new dataset of spaceborne HCHO columns derived from GOME and SCIAMACHY satellite instruments and covering the period 1997–2006 has been compared with corresponding columns calculated with an updated version of the IMAGES global chemical transport model. The main difference between this dataset and previous retrievals lies

in the choice of the fitting window, which reduces retrieval problems over desert areas, while allowing for a good consistency between datasets from the two instruments. Particular emphasis in the comparisons has been placed on the continental Tropics, where HCHO abundances are generally dominated by biogenic and pyrogenic NMVOC emissions, and on North America and China, experiencing strong biogenic emissions during the growing season. Two biomass burning inventories (GFEDv1 and v2) and two biogenic inventories (GEIA and MEGAN-ECMWF) are evaluated with IMAGESv2 through comparisons between observed and simulated monthly averaged HCHO columns. The NMVOC chemical mechanism has been adjusted and extended on the basis of box model simulations conducted using the MCM mechanism for the most prominent pyrogenic NMVOCs. Three model simulations have been carried out using the following combinations of inventories: GFEDv1/GEIA (S1), GFEDv1/MEGAN-ECMWF (S2), and GFEDv2/MEGAN-ECMWF (S3).

The high correlation coefficients computed between the (monthly averaged) simulated and retrieved columns provide strong confidence in both the model and the emission inventories used. The use of MEGAN-ECMWF is found to improve the correlation between model and data over all regions of Fig. 7, suggesting that this inventory provides a much better representation of the temporal variability in the emissions.

Whereas for biogenic emissions the comparisons allowed to assess the better performance of the MEGAN-based inventory, the situation is more complex regarding the biomass burning inventories. In fact, the implementation of GFEDv2 in the model (S3 run) leads to a reduction of the correlation in 9 out of the 20 selected regions, located mostly in South America, but to an increase in 8 regions, in particular in Indonesia, N. Australia and Southern Africa. Although neither GFED version appears to be consistent with the observation over all regions, the differences between these two inventories can be evaluated based on these model/data comparisons. For instance, the significance of emissions associated with peat bog fires included in GFEDv2 is supported by the observations, since they result in a better seasonal variation over Indonesia, in spite of an overestimation of the modelled columns. Another feature of GFEDv2 corroborated

by the observations is the one-month delay of the emission peak over Southern Africa, induced by the use of MODIS hot spots.

Despite the overall good performance of the two biomass burning databases, it is understood that the use of monthly averaged emissions constitutes a limitation in the comparisons, because of the very high variability of fire emissions. A progress towards the increase of the temporal resolution in the pyrogenic inventories has been performed recently in the GFEDv2, which now provides emission estimates at an 8-day time step over the period 2001–2006. This new feature will be implemented in our future modelling work.

The NMVOC degradation mechanisms used in CTMs constitute another important issue, as demonstrated by the factor of two difference between the HCHO yields from different isoprene degradation mechanisms used in current CTMs. Uncertainties in the chemical mechanism of other biogenic compounds are probably even larger. In addition, OH is believed to be largely underestimated by current models in the boundary layer over the Amazon basin, with possibly important consequences on the modelled HCHO columns. The quantification of this effect will remain difficult as long as the exact causes are not clarified.

Although this study put emphasis on tropical regions, where the detected HCHO signal is strong, anthropogenic NMVOC emissions are also expected to produce a detectable signal in industrialized areas. Anthropogenic NMVOC emissions over North America seem, however, to be undetectable even with the high resolution Ozone Monitoring Instrument (OMI) in summertime (Millet et al., 2008). Their contribution in wintertime is expected to be more significant, though. In order to quantify this contribution based on satellite retrievals, the chemical mechanism of the model should be extended in order to include all anthropogenic precursors of formaldehyde, which should be identified based on a detailed box model study using (quasi-) explicit degradation mechanisms. This issue will be addressed properly in future work. The quantification of the parent NMVOC emissions through inverse modelling should, however, be performed with particular care due to the spatiotemporal overlaps of the different emission source

types.

It is understood that our conclusions depend vitally on the quality of the retrieved columns. However, discrepancies among the retrievals, inherent to differences in the retrieval methods, exist between HCHO datasets. For instance, our GOME slant columns are by about 30–40% lower than the Chance et al. (2000) dataset over North America (Palmer et al., 2006) and desert regions, whereas over central/Southern Africa, HCHO columns used in Meyer-Arnek et al. (2005); Wittrock et al. (2006) are by 40% lower than in the TEMIS dataset. In view of these discrepancies, it is very important to carry out systematic comparisons between the datasets. More efforts should be devoted to validation with ground-based and aircraft data, as well as to the synergistic use of different satellite instruments over the same time period.

Acknowledgements. This work has been supported by the PRODEX programme of the ESA funded by the Belgian Science Policy Office.

References

Abbot, D., Palmer, P. I., Martin, R. V., Chance, K. V., Jacob, D. J., and Guenther, A.: Seasonal and interannual variability of North American isoprene emissions as determined by formaldehyde column measurements from space, Geophys. Res. Lett., 30, 17, doi:10.1029/2003GL017336, 2003. 16984, 17002

Andreae, M. O. and Merlet, P.: Emission of trace gases and aerosols from biomass burning, Global Biogeochem. Cy., 15, 955–966, 2001. 16983, 16991, 17023

Aragão, L. E. O. C., Malhi, Y., Roman-Cuesta, R. M., Saatchi, S., Anderson, L. O., and Shimabukuro, Y. E.: Fingerprints of the 1997/1998 and 2005 droughts and their impact on the susceptibility of Amazonian rainforests to fires, Geophys. Phys. Lett., 34, L07701, doi:10.1029/2006GL028946, 2007. 17004

Atkinson, R.: Gas-phase tropospheric chemistry of organic compounds, J. Phys. Chem. Ref. Data, Monograph No. 2, 1994. 16996

Atkinson, R., Baulch, D. L., Cox, R. A., Crowley, J. N., Hampson, R. F., Hynes, R. G., Jenkin, M. E., Rossi, M. J., Troe, J., et al.: Evaluated kinetic and photochemical data for atmospheric

chemistry: Volume II – gas phase reactions of organic species, Atmos. Chem. Phys., 6, 3625–4055, 2006, http://www.atmos-chem-phys.net/6/3625/2006/. 16997
Boersma, K. F., Eskes, H. J., and Brinksma, E. J.: Error analysis for tropospheric NO_2 retrieval from space, J. Geophys. Res., 109, D04311, doi:10.1029/2003JD003962, 2004. 16988
Brasseur, G. P., Orlando, J. J., and Tyndall, G. S.: Atmospheric Chemistry and Global Change, Oxford University Press, 654 pp., 1999. 16983
Cantrell C. A., Davidson, J. A., McDaniel, A. H., Shetter, R. E., and Calvert, J. G.: Temperature-dependent formaldehyde cross sections in the near-ultraviolet spectral region, J. Phys. Chem., 94, 3902–3908, 1990. 16986, 16989
Chance, K. and Spurr, R. J. D. : Ring effect studies: Rayleigh scattering including molecular parameters for rotational Raman scattering, and the Fraunhofer spectrum, Appl. Optics, 36, 5224–5230, 1997. 16987
Chance, K. V., Palmer, P. I., Spurr, R. J. D., Martin, R. V., Kurosu, T. P., and Jacob, D. J.: Satellite observations of formaldehyde over North America from GOME, Geophys. Res. Lett., 27, 3461–3464, 2000. 16984, 16985, 17002, 17007, 17011
Cronin, L.: Key Guide to Australian Trees, Reed Natural History Australia, 191 pp., 2000. 17008
Damian, V., Sandu, A., Damian, M., Potra, F., and Carmichael, G. R.: The Kinetic PreProcessor KPP – A Software Environment for Solving Chemical Kinetics, Comput. Chem. Eng., 26, 1567–1579, 2002. 16990
Dentener, F., Kinne, S., Bond, T., Boucher, O., Cofala, J., Generoso, S., Ginoux, P., Gong, S., Hoelzemann, J. J., Ito, A., Marelli, L., Penner, J. E., Putaud, J.-P., Textor, C., Schulz, M., van der Werf, G. R., and Wilson, J.: Emissions of primary aerosol and precursor gases in the years 2000 and 1750 prescribed data-sets for AeroCom, Atmos. Chem. Phys., 6, 4321–4344, 2006, http://www.atmos-chem-phys.net/6/4321/2006/. 16993
De Smedt, I., Müller, J.-F., Stavrakou, T., van der A, R., Eskes, H., and Van Roozendael, M.: Twelve years of global observations of formaldehyde in the troposphere using GOME and SCIAMACHY sensors, Atmos. Chem. Phys., 8, 4947–4963, 2008, http://www.atmos-chem-phys.net/8/4947/2008/. 16985, 16986, 16988, 16989, 17000, 17002, 17007
Evans, M. J., Fiore, A., and Jacob, D. J.: The GEOS-Chem chemical mechanism version 5-07-8, Harvard University, Cambridge, MA, USA, http://homepages.see.leeds.ac.uk/~lecmje/GEOS-CHEM/geoschem_mech.pdf, 2003. 16997
Fried, A., Walega, J. G., Olson, J. R., Crawford, J. H., Chen, G., Weibring, P., Richter, D., Roller,

C., Tittel, F., Heikes, B. G., Snow, J. A., Shen, H., O'Sullivan, D. W., Porter, M. J., Fuelberg, H. E., Halland, J. J., and Millet, D. B.: Formaldehyde over North America and the North Atlantic during the Summer 2004 INTEX Campaign: Methods, Observed Distributions, and Measurement-Comparisons, J. Geophys. Res., 113, D10302, doi:10.1029/2007JD009185, 2008. 17002

Fu, T.-M., Jacob, D. J., Palmer, P. I., Chance, K., Wang, Y. X., Barletta, B., Blake, D. R., Stanton, J. C., and Pilling, M. J.: Space-based formaldehyde measurements as constraints on volatile organic compound emissions in east and south Asia and implication for ozone, J. Geophys. Res., 112, D06312, doi:10.1029.2006JD007853, 2007. 16984, 16988, 17007

Geron, C., Owen, S., Guenther, A., Greenberg, J., Rasmussen, R., Bai, J. H., Li, Q.-J., and Baker, B.: Volatile organic compounds from vegetation in southern Yunnan Province, China: Emission rates and some potential regional implications, Atmos. Environ., 40, 1759–1773, 2006. 17007

Giglio, L., Kendall, J. D., and Mack, R.: A multi-year active fire dataset for the tropics derived from the TRMM VIRS, Int. J Remote Sens., 24, 22, 4505–4525, 2003. 16991

Giglio, L., van der Werf, G. R., Randerson, J. T., Collatz, G. J., and Kasibhatla, P.: Global estimation of burned area using MODIS active fire observations, Atmos. Chem. Phys., 6, 957–974, 2006, http://www.atmos-chem-phys.net/6/957/2006/. 16991, 16992

Giglio, L.: Characterization of the tropical diurnal fire cycle using VIRS and MODIS observations, Remote Sense Environ., 108, 407–421, 2007. 16993

Grainger, J. F. and Ring, J.: Anomalous Fraunhofer line profiles, Nature, 193, 762 pp., 1962. 16987

Guenther, A., Hewitt, C. N., Erickson, D., Fall, R., Geron, C., Graedel, T., Harley, P., Klinger, L., Lerdau, M., McKay, W. A., Pierce, T., Scholes, B., Steinbrecher, R., Tallamraju, R., Taylor, J., and Zimmerman, P.: A global model of natural volatile organic compound emissions, J. Geophys. Res., 100, 8873–8892, 1995. 16983, 16985, 16994, 17003, 17022

Guenther, A., Karl, T., Harley, P., Wiedinmyer, C., Palmer, P. I., and Geron, C.: Estimates of the global terrestrial isoprene emissions using MEGAN (Model of Emissions of Gases and Aerosols from Nature), Atmos. Chem. Phys., 6, 3181–3210, 2006, http://www.atmos-chem-phys.net/6/3181/2006/. 16985, 16993, 16994, 17006, 17007, 17022

He, C., Murray, F., and Lyons, T.: Monoterpene and isoprene emissions from 15 *Eucalyptus* species in Australia, Atmos. Environ., 34, 645–655, 2000. 17008

Heikes, B., Snow, J., Egli, P., O'Sullivan, D., Crawford, J., Olson, J., Chen, G., Davis, D., Blake,

N., and Blake, D.: Formaldehyde over the central Pacific during PEM-Tropics B, J. Geophys. Res., 106, D23, 32 717–32 731, 2001. 17003

Houweling, S., Dentener, F., and Lelieveld, J.: The impact of non-methane hydrocarbon compounds on tropospheric photochemistry, J. Geophys. Res., 103, 10 673–10 696, 1998. 16983

Jacob, D. J., Field, B. D., Li, Q., Blake, D. R., de Gouw, J., Warneke, C., Hansel, A., Wisthaler, A., Singh, H. B., and Guenther, A.: Global budget of methanol: constraints from atmospheric observations, J. Geophys. Res., 110, D08303, doi:10.1029/2004JD005172, 2005. 16995

Justice, C. O., Giglio, L., Korontzi, S., Owens, J., Morisette, J. T., Roy, D., Descloitres, J., Alleaume, S., Petitcolin, F., and Kaufman, Y.: The MODIS fire products, Remote Sens. Environ., 83, (1–2), 244–262, 2002. 16991

Karl, T., Guenther, A., Yokelson, R. J., Greenberg, J., Potosnak, M., Blake, D. R., and Artaxo, P.: The tropical forest and fire emissions experiment: Emission, chemistry, and transport of biogenic volatile organic compounds in the lower atmosphere over Amazonia, J. Geophys. Res., 112, D18302, doi:10.1029/2007JD008539, 2007. 16984

Khokhar, M. F., Frankenberg, C., Van Roozendael, M., Beirle, S., Kühl, S., Richter, A., Platt, U., and Wagner, T.: Satellite observations of atmospheric SO_2 from volcanic eruptions during the time period of 1996 to 2002, Adv. Space Res., 36(5), 879–887, doi:10.1016/j.asr.2005.04.114, 2005. 16987

Koelemeijer, R. B. A., Stammes, P., Hovenier, J. W., and de Haan, J. F.: Global distributions of effective cloud fraction and cloud top pressure derived from oxygen A band spectra measured by the Global Ozone Monitoring Experiment: comparison to ISCCP data, J. Geophys. Res., 107, D12, 4151, doi:10.1029/2001JD000840, 2002. 16988

Koelemeijer, R. B. A., de Haan, J. F., and Stammes, P.: A database of spectral surface reflectivity in the range 335–772 nm derived from 5.5 years of GOME observations, J. Geophys. Res., 108, D2, 4070, doi:10.1029/2002JD002429, 2003. 16988

Kuhn, U., Andreae, M. O., Ammann, C., Araújo, A. C., Brancaleoni, E., Ciccioli, P., Dindorf, T., Frattoni, M., Gatti, L. V., Ganzeveld, L., Kruijt, B., Lelieveld, J., Lloyd, J., Meixner, F. X., Nobre, A. D., Pöschl, U., Spirig, C., Stefani, P., Thielmann, A., Valentini, R., and Kesselmeier, J.: Isoprene and monoterpene fluxes from Central Amazonian rainforest inferred from tower-based and airborne measurements, and implications on the atmospheric chemistry and the local carbon budget, Atmos. Chem. Phys., 7, 2855–2879, 2007, http://www.atmos-chem-phys.net/7/2855/2007/. 16984

Kylling, K., Stammes, P., and Tsay, S. C.: A reliable and efficient two-stream algorithm for

spherical radiative transfer: Documentation of accuracy in realistic layered media, J. Atmos. Phys., 21, 115–150, 1995. 16988

Lelieveld, J., Butler, T. M., Crowley, J. N., Dillon, T. J., Fischer, H., Ganzeveld, L., Harder, H., Lawrence, M. G., Martinez, M., Taraborelli, D., and Williams, J.: Atmospheric oxidation capacity sustained by a tropical forest, Nature, 452, 737–740, 2008. 16984

Li, Q., Jacob, D. J., Yantosca, R. M., Heald, C. L., Singh, H. B., Koike, M., Zhao, Y., Sachse, G. W., and Streets, D. G.: A global three-dimensional model analysis of the atmospheric budgets of HCN and CH_3CN: constraints from aircraft and ground measurements, J. Geophys. Res., 108, D21, 8827, doi:10.1029/2002JD003075, 2003. 17020

Madronich, S. and Flocke, S.: The role of solar radiation in atmospheric chemistry, in: Handbook of Environmental Chemistry, edited by: Boule, P., Springer Verlag, Heidelberg, 1–26, 1998. 16994

Marengo, J. A., Nobre, C. A., Tomasella, J., Oyama, M. D., de Oliveira, G. S., de Oliveira, R., Camargo, H., Alves, L. M., and Brown, I. F.: The drought of Amazonia in 2005, J. Climate, 21, 495–516, 2008. 17004

Martin, R. V., Chance, K., Jacob, D. J., Kurosu, T. P., Spurr, R. J. D., Bucsela, E., Gleason, J. F., Palmer, P. I., Bey, I., Fiore, A. M., Li, Q., Yantosca, R. M., and Koelemeijer, R. B. A.: An improved retrieval of tropospheric nitrogen dioxide from GOME, J. Geophys. Res., 107, D20, doi:10.1029/2001JD001027, 2001. 16988

Martin, R. V., Jacob, D. J., Chance, K. V., Kurosu, T. P., Palmer, P. I., and Evans, J.: Global inventory on nitrogen dioxide emissions constrained by space-based observations of NO_2 Columns, J. Geophys. Res., 108, D17, doi:10.1029/2003JD003453, 2003. 16988

Meller, R. and Moortgat, G. K. : Temperature dependence of the absorption cross section of HCHO between 223 and 323 K in the wavelength range 225–375 nm, J. Geophys. Res., 105, D6, 7089–7102, doi:10.1029/1999JD901074, 2000. 16989

Meyer-Arnek, J., Ladstätter-Weißenmayer, A., Richter, A., Wittrock, F., and Burrows, J. P.: A study of trace gas columns of O_3, NO_2 and HCHO over Africa in September 1997, Faraday Discuss., 130, 387–405, 2005. 17011

Millet, D. B., Jacob, D. J., Turquety, S., Hudman, R. C., Wu, S., Fried, A., Walega, J., Heikes, B. G., Blake, D. R., Singh, H. B., Anderson, B. E., and Clarke, A. D.: Formaldehyde distribution over North America: implications for satellite retrievals of formaldehyde columns and isoprene emission, J. Geophys. Res., 111, D24S02, doi:10.1029/2005JD006853, 2006. 16997, 17003

Millet, D. B., Jacob, D. J., Fu, T.-M., Kurosu, T. P., Chance, K., Heald, C. L., and Guenther, A.: Spatial distribution of isoprene emissions from North America derived from formaldehyde column measurements by the OMI satellite sensor, J. Geophys. Res., 113, D02307, doi:10.1029/2007JD008950, 2008. 16984, 17002, 17010

Müller, J.-F. and Stavrakou, T.: Inversion of CO and NO_x emissions using the adjoint of the IMAGES model, Atmos. Chem. Phys., 5, 1157–1186, 2005, http://www.atmos-chem-phys.net/5/1157/2005/. 16983, 16985, 16990, 16995, 16999

Müller, J.-F., Stavrakou, T., Wallens, S., De Smedt, I., Van Roozendael, M., Potosnak, M., Rinne, J., Munger, B., Goldstein, A., and Guenther, A. B.: Global isoprene emissions estimates using MEGAN, ECMWF analyses and a detailed canopy environment model, Atmos. Chem. Phys., 8, 1329–1341, 2008, http://www.atmos-chem-phys.net/8/1329/2008/. 16985, 16993, 16994, 17004, 17005, 17008, 17022

Olivier, J .G. J., Berdowski, J. J. M., Peters, J. A. H. W., Bakker, J., Visschedijk, A. J. H., and Bloos, J.-P. J.: Applications of EDGAR. Including a description of EDGAR 3.0: reference database with trend data for 1970-1995, RIVM report no. 773301 001/ NOP report no. 410200 051, RIVM, Bilthoven, 2001. 16983, 16991

Olivier, J .G. J.: Part III: Greenhouse gas emissions. 1. Shares and trends in greenhouse gas emissions; 2. Sources and methods: greenhouse gas emissions for 1990 and 1995 in "CO_2 emissions from fuel combustion 1971–2000", 1–31, International Energy Agency, Paris, ISBN 92-64-09794-5, 2002. 16991

Olivier, J .G. J., Peters, J., Granier, C., Pétron, G., Müller, J.-F., and Wallens, S.: Present and future surface emissions of atmospheric compounds, POET Report 2, EU project EVK2-1999-00011, 2003. 16983, 16991

Otter, L., Guenther, A., Wiedinmyer, C., Fleming, G., Harley, P., and Greenberg, J.: Spatial and temporal variations in biogenic volatile organic compound emissions for Africa south of the equator, J. Geophys. Res., 108, D13, 8505, doi:10.1029/2002JD002609, 2003. 17005

Palmer, P. I., Jacob, D. J., Chance, K., Martin, R. V., Spurr, R. J. D., Kurosu, T. P., Bey, I., Yantosca, R., Fiore, A., and Li, Q.: Air-mass factor formulation for spectroscopic measurements from satellites: application to formaldehyde retrievals from GOME, J. Geophys. Res., 106, 14 539–14 550, 2001. 16987

Palmer, P., Abbot, D. S., Fu, T.-M., Jacob, D. J., Chance, K., Kurosu, T. P., Guenther, A., Wiedinmyer, C., Stanton, J. S., Pilling, M. J., Pressley, S. N., Lamb, B., and Summer, A. L.: Quantifying the seasonal and interannual variability of North American isoprene emissions

using satellite observations of the formaldehyde column, J. Geophys. Res., 111, D12315, doi:10.1029/2005JD006689, 2006. 16984, 16997, 16998, 17002, 17003, 17011

Palmer, P. I., Barkley, M. P., Kurosu, T. P., Lewis, A. C., Saxton, J. E., Chance, K., and Gatti, L. V.: Interpreting satellite column observations of formaldehyde over tropical South America, Phil. Trans. R. Soc. A., 365, 1741–1751, 2007. 16984

Peeters, J., Vereecken, L., and Fantechi, G.: The detailed mechanism of the OH-initiated atmospheric oxidation of alpha-pinene: a theoretical study, Phys. Chem. Chem. Phys., 3, 5489–5504, 2001. 16984, 16998

Pfister, G., Emmons, L. K., Hess, P. G., Lamarque, J.-F., Walters, S., Guenther, A., Palmer, P. I., and Lawrence, P.: Contribution of isoprene to chemical budgets: A model tracer study with the NCAR CTM MOZART-4, J. Geophys. Res., 113, D05308, doi:10.1029/2007JD008948, 2008. 16983

Pinho, P. G., Pio, C. A., and Jenkin, M. E.: Evaluation of isoprene degradation in the detailed tropospheric chemical mechanism, MCM v3, using environmental chamber data, Atmos. Environ., 39, 1303–1322, 2005. 16997

Platt, U.: Differential Optical Absorption Spectroscopy (DOAS), in: Air Monitoring by Spectroscopic Techniques, edited by: Sigrist, M. W. John Wiley & Sons, Inc., New York, 1994. 16986

Pöschl, U., von Kuhlmann, R., Poisson, N., and Crutzen, P. J.: Development and intercomparison of condensed isoprene oxidation mechanisms for global atmospheric modeling, J. Atmos. Chem., 37, 29–52, 2000. 16995

Richter, A. and Wagner, T.: Diffuser plate spectral structures and their influence on GOME slant columns, Tech. Note, Bremen Univ. and Heidelberg Univ., 2001. 16987

Rossow, W. B., Walker, A. W., Beuschel, D. E., and Roiter, M. D.: International Satellite Cloud Climatology Project (ISCCP) Documentation of New Cloud Datasets, Report WMO/TD-No. 737, World Meteorological Organization, Geneva, 115 pp., 1996. 16994

Sander, S. P., Finlayson-Pitts, B. J., Friedl, R. R., Golden, D. M., Huie, R. E., Keller-Rudek, H., Kolb, C. E., Kurylo, M. J., Molina, M. J., Moortgat, G. K., Orkin, L. V., Ravishankara, A. R., and Wine, P. H.: Chemical Kinetics and Photochemical data for use in atmospheric studies, Evaluation number 15, NASA Panel for data evaluation, JPL Publication 06-2, Jet Propulsion Laboratory, Pasadena, 2006. 16995, 16996, 16998

Sandu, A. and Sander, R.: Technical Note: Simulating chemical systems in Fortran90 and Matlab with the Kinetic PreProcessor KPP-2.1, Atmos. Chem. Phys., 6, 187–195, 2006,

http://www.atmos-chem-phys.net/6/187/2006/. 16990
Saunders, S. M., Jenkin, M. E., Derwent, R. G., and Pilling, M. J.: Protocol for the development of the Master Chemical Mechanism, MCM v3 (Part A): tropospheric degradation of non-aromatic volatile organic compounds, Atmos. Chem. Phys., 3, 161–180, 2003, http://www.atmos-chem-phys.net/3/161/2003/. 16984, 16995, 16996, 17020
Singh H. B., Brune, W. H., Crawford, J. H., Jacob, D. J., and Russell, P. B.: Overview of the summer 2004 Intercontinental Chemical Transport Experiment North America (INTEX-A), J. Geophys. Res., 111, D24S01, doi:10.1029/2006JD007905, 2006. 17002
Shim, C., Yang, Y., Choi, Y., Palmer, P. I., Abbot, D., and Chance, K.: Constraining global isoprene emissions with Global Ozone Monitoring Experiment (GOME) formaldehyde column measurements, J. Geophys. Res., 110, D24301, doi:10.1029/2004JD005629, 2005. 16984, 17004
Smolarkiewicz, P. K. and Rasch, P. J.: Monotone advection on the sphere: An Eulerian versus semi-Lagrangian approach, J. Atmos. Sci., 48, 793–810, 1991. 16990
Stammes, K., Tsay, S. C., Wiscombe, W., and Jayaweera, K.: Numerically stable algorithm for discrete-ordinate-method radiative transfer in multiple scattering and emitting layered media, Appl. Optics, 27, 2505–2509, 1988. 16988
Stavrakou, T. and Müller, J.-F.: Grid-base versus big region approach for inverting CO emissions using Measurement of Pollution in the Troposphere (MOPITT) data, J. Geophys. Res., 111, D15304, doi:10.1029/2005JD006896, 2006. 17006
Trostdorf, C. R., Gatti, L. V., Yamazaki, A., Potosnak, M. J., Guenther, A., Martins, W. C., and Munger, J. W.: Seasonal cycles of isoprene concentrations in the Amazonian rainforest, Atmos. Chem. Phys. Discuss., 4, 1291–1310, 2004, http://www.atmos-chem-phys-discuss.net/4/1291/2004/. 17004
Tyndall, G. S., Orlando, J. J., Wallington, T. J., and Hurley, M. D.: Products of the chlorine-atom- and hydroxyl-radical-initiated oxidation of CH_3CN, J. Phys. Chem. A, 105, 5380–5384, 2001. 17020
Uppala, S. M., Kallberg, P. W., Simmons, A. J., et al.: The ERA-40 re-analysis, Q. J. Roy. Meteor. Soc., 131, 2961–3012, doi:10.1256/qj.04.176., 2005. 16990
van der Werf, G. R., Randerson, J. T., Collatz, G. J., and Giglio, L.: Carbon emissions from fires in tropical and subtropical ecosystems, Glob. Change Biol., 9, 547–562, 2003. 16991, 17023
van der Werf, G. R., Randerson, J. T., Collatz, G. J., Giglio, L., Kasibhatla, P. S., Arellano, A. F.,

Jr., Olsen, S. C., and Kasischke, E. S.: Continental scale partitioning of fire emissions during the 1997 to 2001 El Niño/La Niña period, Science, 303, 73–76, 2004. 16985, 16991, 17022

van der Werf, G. R., Randerson, J. T., Giglio, L., Collatz, G. J., Kasibhatla, P. S., and Arellano, Jr., A. F.: Interannual variability in global biomass burning emissions from 1997 to 2004, Atmos. Chem. Phys., 6, 3423–3441, 2006, http://www.atmos-chem-phys.net/6/3423/2006/. 16985, 16991, 17022, 17024

Van Roozendael, M., Fayt, C., Lambert, J.-C., Pundt, I., Wagner, T., Richter, A., and Chance, K.: Development of a bromine oxide product from GOME, in Proc. ESAMS'99, WPP-161, 543–547, 1999. 16986

Vereecken, L., Müller, J.-F., and Peeters, J.: Low-volatility poly-oxygenates in the OH-initiated atmospheric oxidation of α-pinene: impact of non-traditional peroxyl radical chemistry Phys. Chem. Chem. Phys., 9, 5241–5248, doi:10.1039/b708023a, 2007. 16984

Wallens, S.: Modélisation des émissions des composés organiques volatils par la végétation, Ph. D. Thesis, Université Libre de Bruxelles, 2004. 16993

Wang, P., Stammes, P., van der A, R., Pinardi, G., and van Roozendael, M.: FRESCO+: an improved O_2 A-band cloud retrieval algorithm for tropospheric trace gas retrievals, Atmos. Chem. Phys. Discuss., 8, 9697–9729, 2008, http://www.atmos-chem-phys-discuss.net/8/9697/2008/. 16988

Wittrock, F., Richter, A., Ladstätter-Weißenmayer, A., and Burrows, J. P.: Global observations of formaldehyde, Proc. ERS-ENVISAT Symposium, ESA-Publ. SP-461, 2000. 16985

Wittrock F., Richter, A., Oetjen, H., Burrows, J. P., Kanakidou, M., Myriokefalitakis, S., Volkamer, R., Beirle, S., Platt, U., and Wagner, T. : Simultaneous global observations of glyoxal and formaldehyde from space, Geophys. Res. Lett., 33, L16804, doi:10.1029/2006GL026310, 2006. 16985, 17011

Zhang, P., Anderson, B., Barlow, M., Tan, B., and Myneni, R.: Climate related vegetation characteristics derived from MODIS LAI and NDVI, J. Geophys. Res., 109, D20105, doi:10.1029/2004JD004720, 2004. 16994

Table 1. Photochemical production of HCHO from pyrogenic NMVOCs and from biogenic isoprene. The emission estimates are 10-year averages based on GFEDv2 and the MEGAN/ECMWF inventory. Short-term and final yields are obtained from box model simulations (see text for details). Note: a. This total includes 10 Tg/year of compounds with negligible HCHO yields: formic acid and acetylene (Saunders et al., 2003), hydrogen cyanide (Li et al., 2003), and acetonitrile (Tyndall et al., 2001).

	NMVOC Emission	MCM HCHO Yield (mol/mol)		IMAGESv2 HCHO Yield (mol/mol)		MCM HCHO Production (Tg/yr)	
	(Tg/yr)	Sh.-term	Final	Sh.-term	Final	Sh.-term	Final
Acetic acid	17.1	0.12	1	0.11	1	1.03	8.54
Methanol	8.8	0.14	1	0.14	1	1.15	8.28
Ethene	6.3	1.38	1.76	1.33	1.76	9.34	11.92
Glyoxal	6.0	0.06	0.06	0.06	0.06	0.19	0.19
Formaldehyde	5.0	1	1	1	1	5.04	5.04
Glycolaldehyde	4.8	0.80	0.87	0.76	0.88	1.92	2.10
Methylglyoxal	3.9	1	1	1	1	1.63	1.63
2,3-butanedione	3.7	2	2	2	2	2.55	2.55
Acetaldehyde	3.6	0.94	1	0.94	1	2.25	2.40
Propene	3.5	1.78	1.92	1.80	1.95	4.34	4.68
Ethane	3.2	0.03	0.99	0.03	0.99	0.09	3.21
Acetone	3.0	0.11	2	0.10	2	0.18	3.18
Propane	1.9	0.03	1.65	0.03	1.62	0.04	2.15
2-butanone	1.7	0.53	2.15	0.49	1.99	0.38	1.54
Benzene	1.7	0.05	0.31	–	–	0.03	0.20
Toluene	1.0	0.62	1.34	–	–	0.21	0.46
Others	20.8[a]					5.04	7.60
Total pyrogenic	**96**					**35**	**66**
Isoprene	**410**	2.26	2.58	2.32	2.64	**479**	**547**

Table 2. Comparison between the MCM and IMAGESv2 computed HCHO molar yields from isoprene under low NO_x (0.1 ppbv NO_2) and high NO_x (1 ppbv NO_2) conditions.

HCHO yield from isoprene	Short-term (mol/mol)		Final (mol/mol)	
NO_2 concentrations	0.1 ppbv NO_2	1 ppbv NO_2	0.1 ppbv NO_2	1 ppbv NO_2
MCM	2.05	2.26	2.46	2.58
IMAGESv2	1.96	2.32	2.32	2.64

Table 3. Simulations conducted with the global model.

Sim.	*Prior pyrogenic emissions*	*Prior biogenic emissions*
S1	GFEDv1 (van der Werf et al., 2004)	GEIA (Guenther et al., 1995)
S2	GFEDv1	MEGAN-ECMWF (Guenther et al., 2006) (Müller et al., 2008)
S3	GFEDv2 (van der Werf et al., 2006)	MEGAN-ECMWF

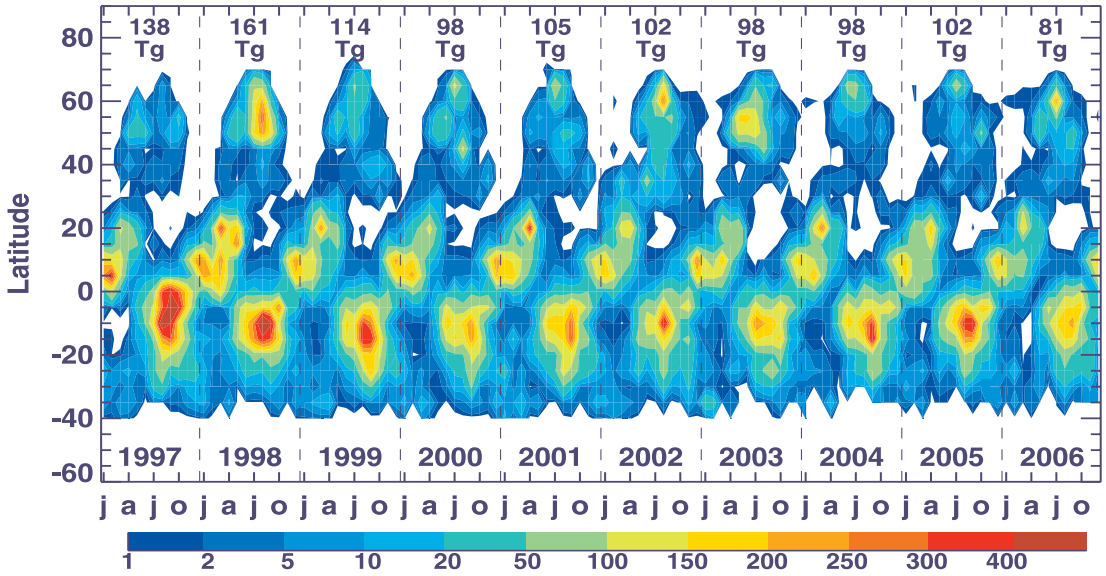

Fig. 1. Zonal distribution of the monthly mean NMVOC emissions calculated using the emission factors provided by Andreae and Merlet (2001) with updates from M.O. Andreae (personal communication, 2007) and the global biomass burnt estimate from the GFEDv1 database (van der Werf et al., 2003).

ACPD
8, 16981–17036, 2008

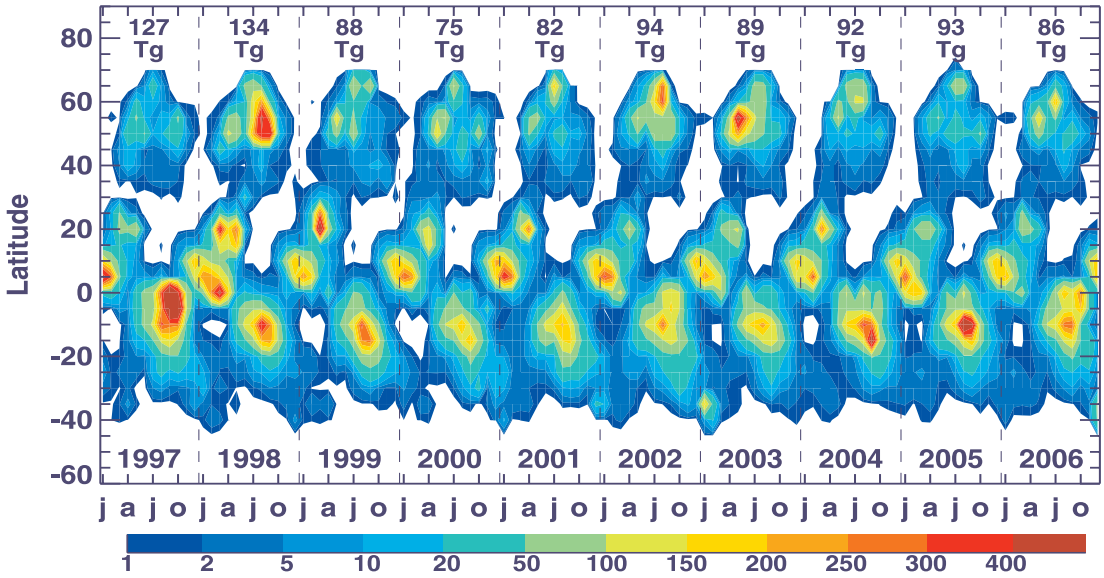

Fig. 2. Same as in Fig. 1 but for the GFEDv2 database (van der Werf et al., 2006).

ACPD
8, 16981–17036, 2008

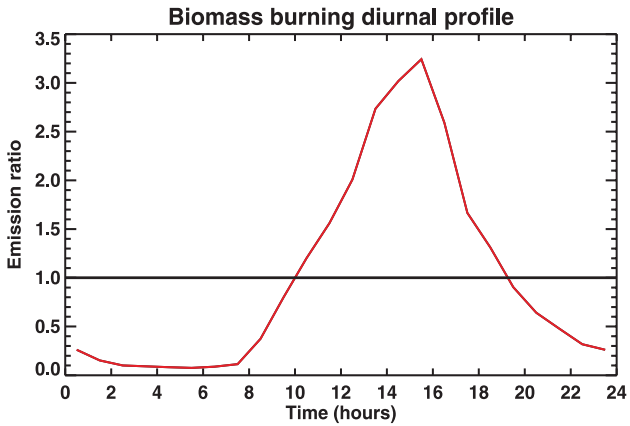

Fig. 3. Average diurnal fire cycle. The black line corresponds to an absence of cycle in pyrogenic emissions.

ACPD
8, 16981–17036, 2008

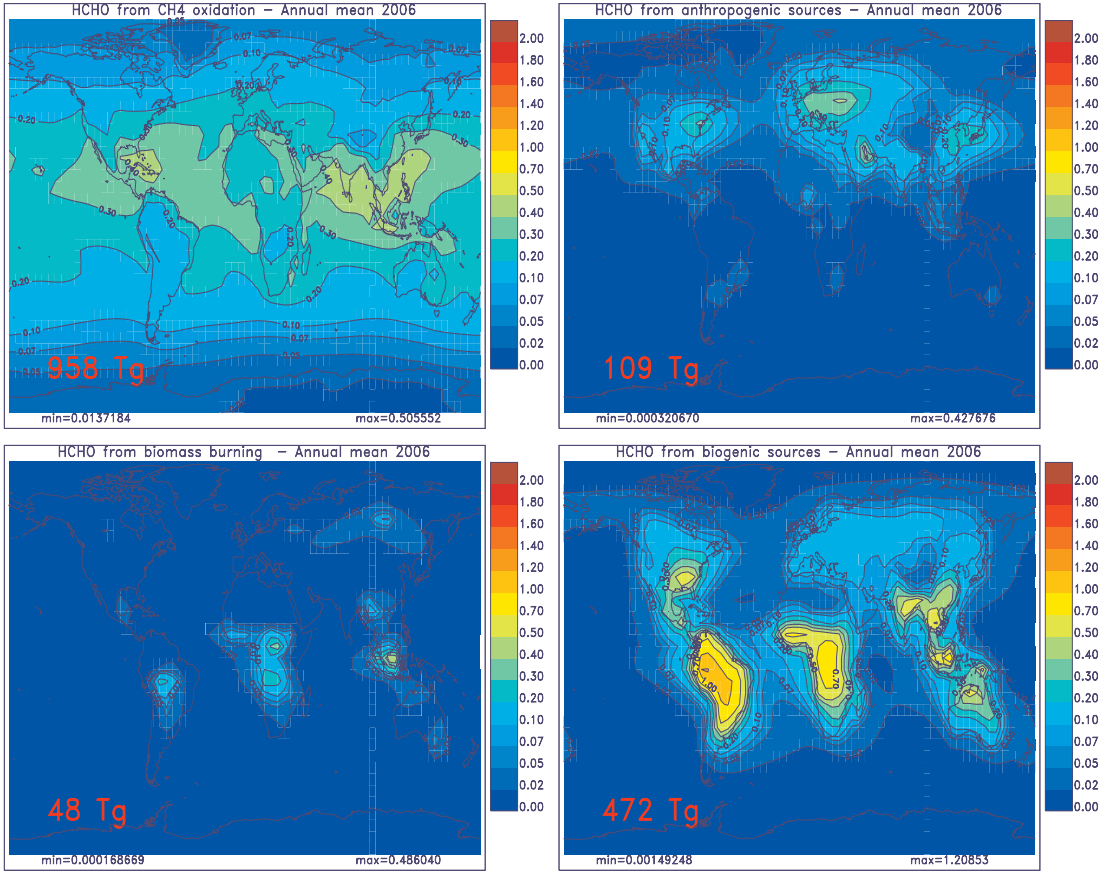

Fig. 4. Contributions to the total modelled HCHO columns (averaged over 2006) by different emission sources: **(a)** CH_4 oxidation (including also a small oceanic source of NMVOCs),**(b)** anthropogenic, **(c)** pyrogenic, and **(d)** biogenic NMVOCs oxidation. Units are 10^{16} molec.cm^{-2}. The global amount of HCHO produced annually by the corresponding source is indicated inset.

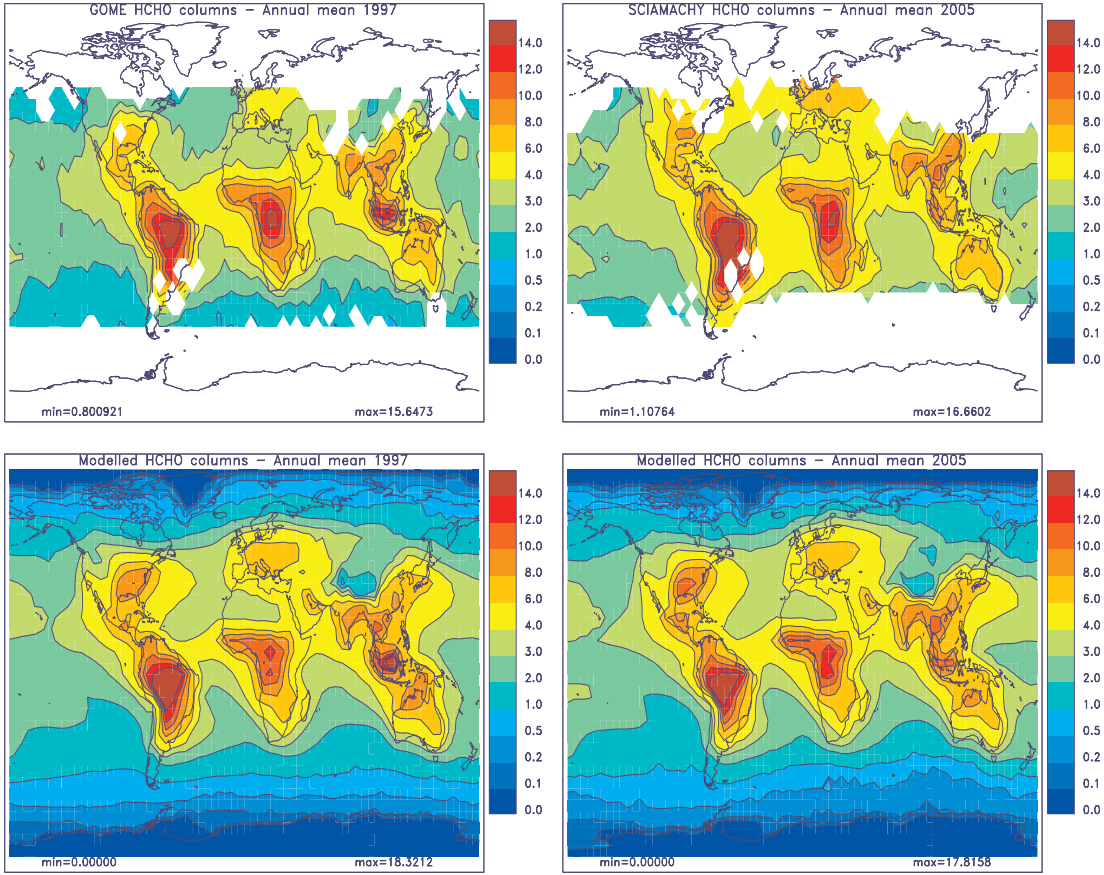

Fig. 5. HCHO columns retrieved from GOME in 1997 and SCIAMACHY in 2005 and calculated using IMAGESv2 with the GFEDv1 biomass burning inventory and biogenic emissions from MEGAN-ECMWF. Units are 10^{15} molec.cm^{-2}. Blank regions in the upper panels denote a lack of valid data (e.g. missing cloud cover information, South Atlantic Anomaly, large zenith angles).

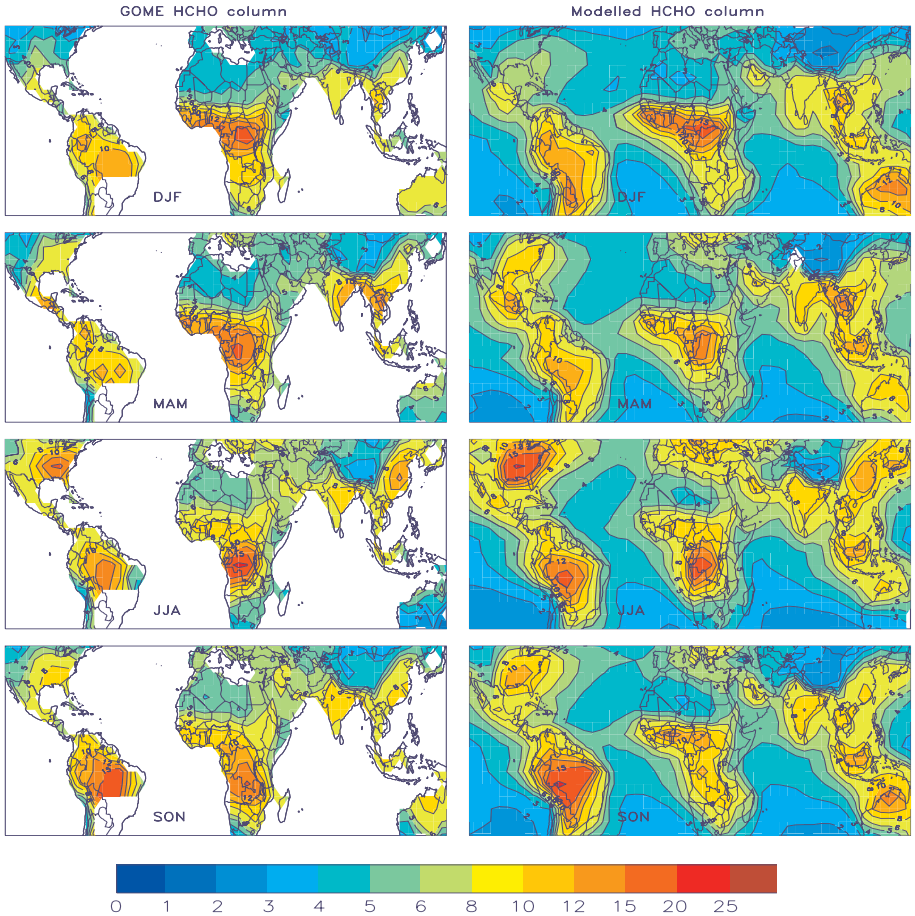

Fig. 6. Seasonally averaged HCHO columns retrieved from GOME in 2000 (left panels) and calculated columns using the GFEDv1 biomass burning inventory and biogenic emissions from MEGAN-ECMWF (right panels). Units are 10^{15} molec.cm^{-2}.

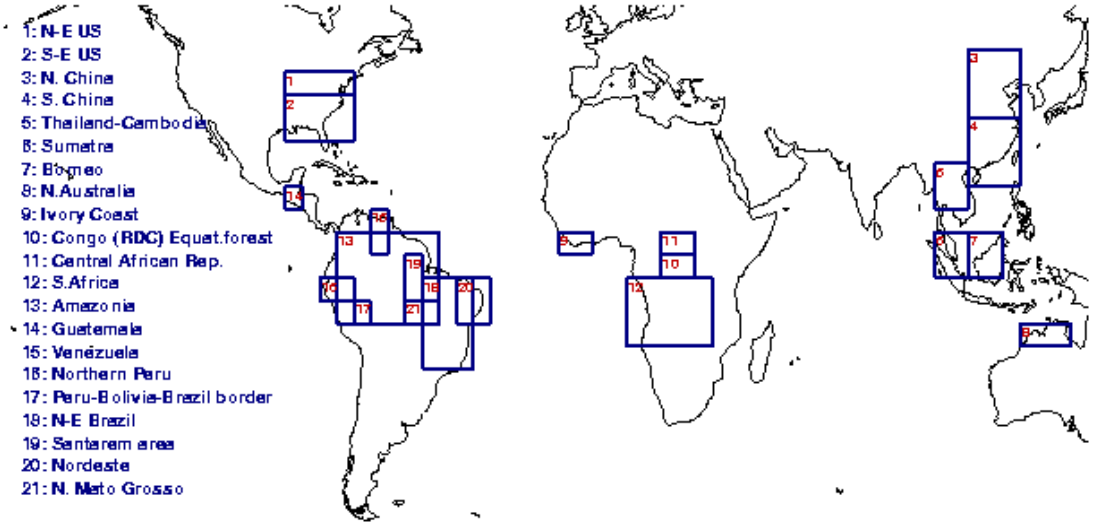

Fig. 7. Regions where the model is confronted to the observations (Fig. 10–Fig. 13).

ACPD
8, 16981–17036, 2008

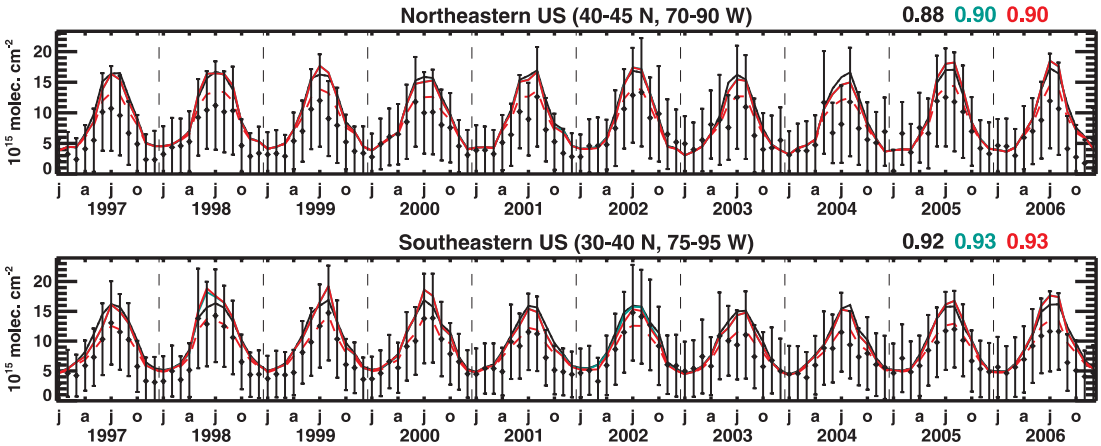

Fig. 8. Comparison between monthly averaged modelled and observed columns over the eastern US. Line codes are as follows: S1 (GFEDv1/GEIA) in black, S2 (GFEDv1/MEGAN-ECMWF) in green, S3 (GFEDv2/MEGAN-ECMWF) in red. The correlation coefficients for each simulation are indicated on the right of each plot. The dashed red curve denote results obtained with halved biogenic MEGAN-ECMWF emissions.

ACPD
8, 16981–17036, 2008

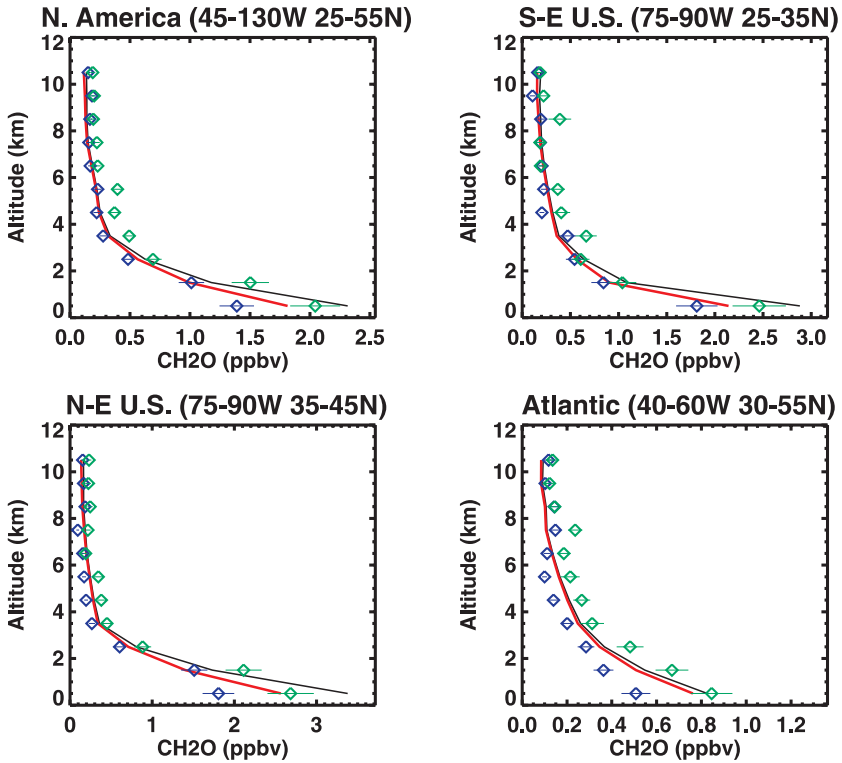

Fig. 9. Mean simulated and observed vertical distributions during INTEX-A (July–August 2004). Blue and green symbols correspond to the URI (Univ. Rhode Island) and NCAR (Colorado) datasets, respectively. Black solid lines are from the simulation using GFEDv1 and MEGAN-ECMWF (S2), whereas red lines from a simulation where the MEGAN-ECMWF source is halved.

ACPD
8, 16981–17036, 2008

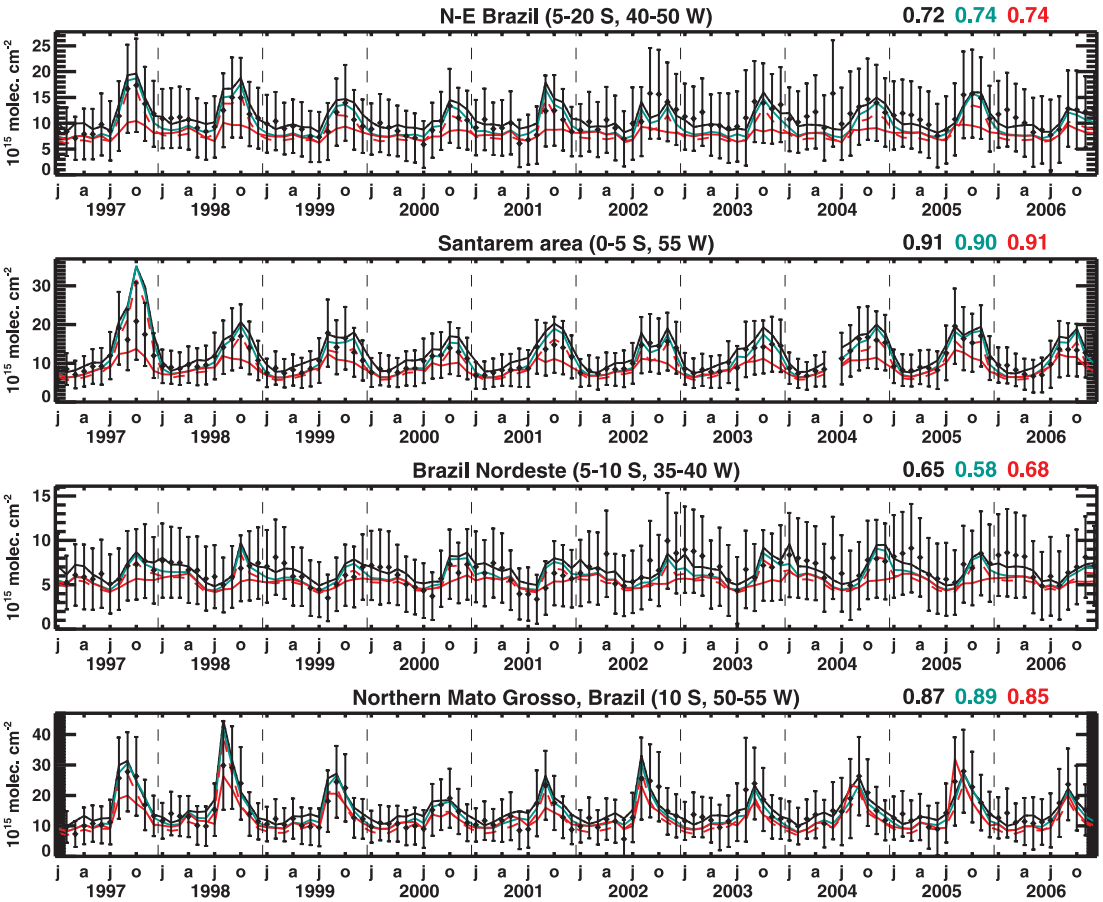

Fig. 10. Comparison between monthly averaged modelled and observed columns over four regions in Brazil. Line colors are as in Fig. 10.

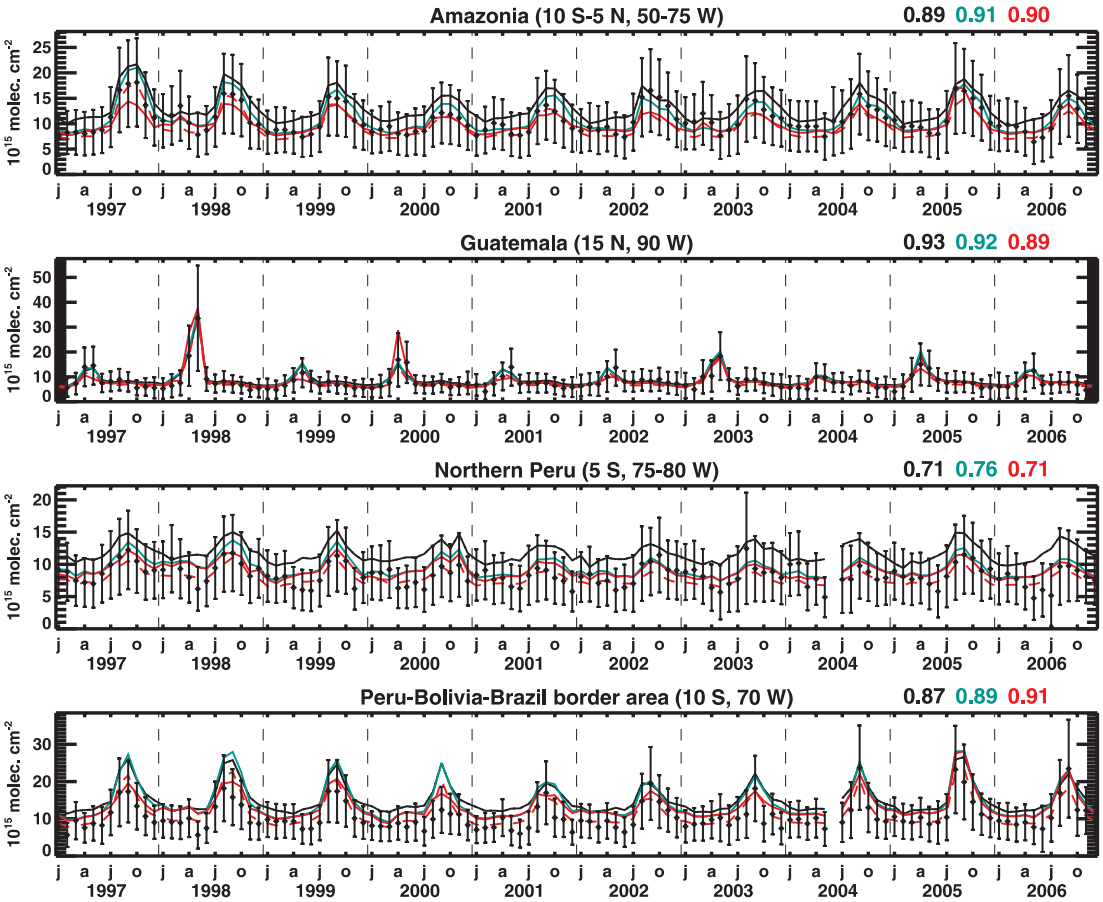

Fig. 11. Modelled vs. observed columns over four regions in Tropical America. Line colors are as in Fig. 10.

ACPD
8, 16981–17036, 2008

NMVOC emissions vs. spaceborne HCHO columns

T. Stavrakou et al.

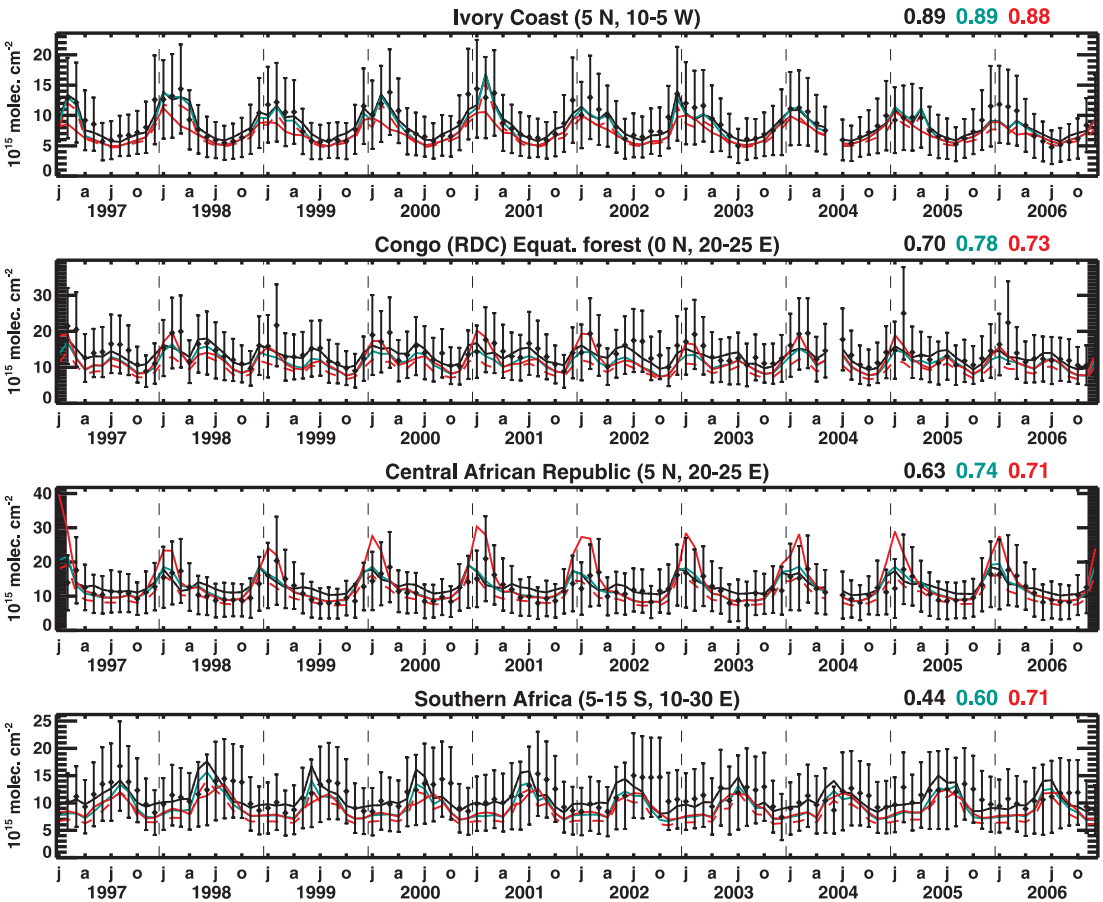

Fig. 12. Monthly averaged modelled and observed columns at four African regions. Line colors are as in Fig. 10.

ACPD
8, 16981–17036, 2008

NMVOC emissions vs. spaceborne HCHO columns

T. Stavrakou et al.

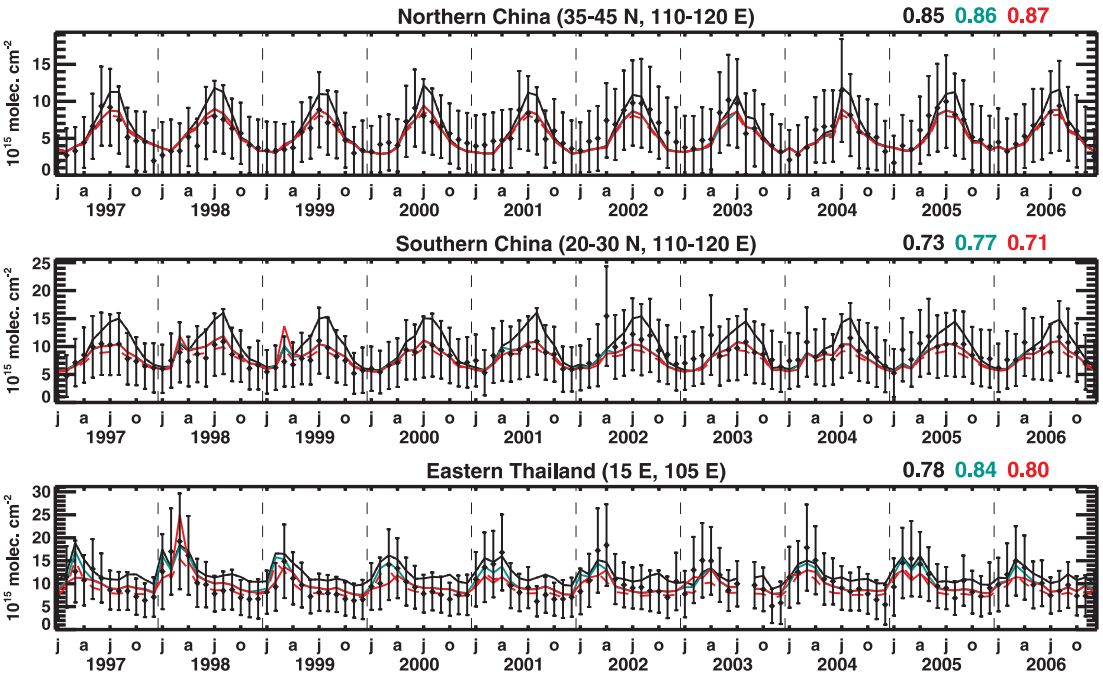

Fig. 13. Monthly averaged modelled and observed columns over three regions in east Asia. Line colors are as in Fig. 10.

ACPD
8, 16981–17036, 2008

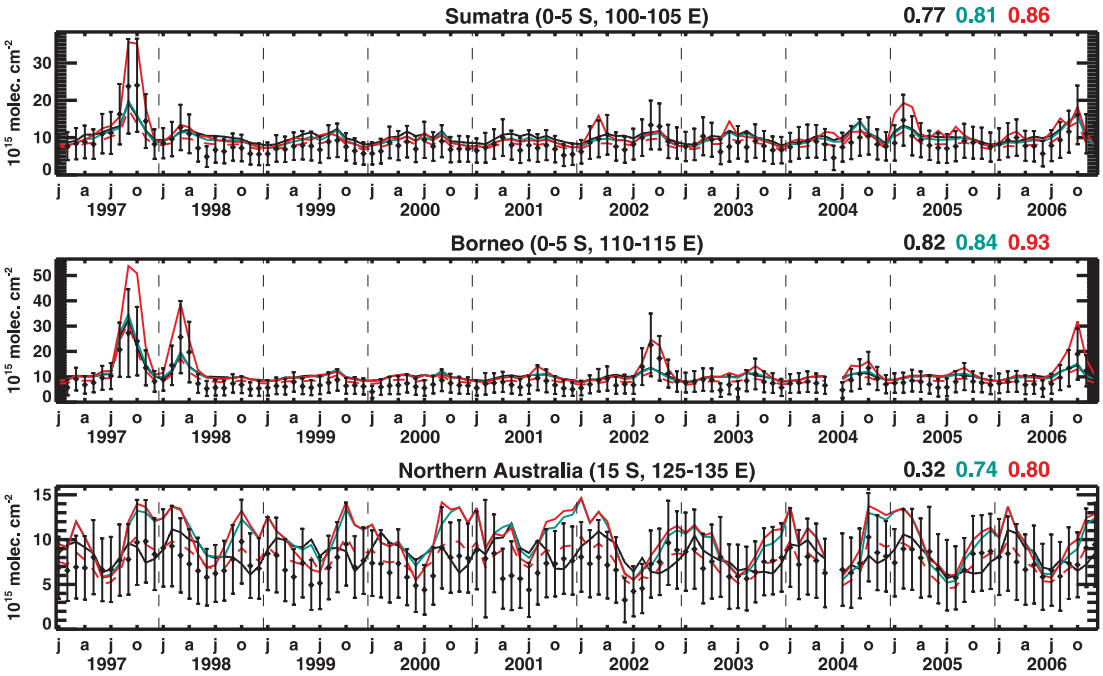

Fig. 14. Monthly averaged modelled and observed columns over Sumatra, Borneo and northern Australia. Line colors are as in Fig. 10.